

Observational Techniques With Transiting Exoplanetary Atmospheres

David K. Sing

Transiting exoplanets provide detailed access to their atmospheres, as the planet's signal can be effectively separated from that of its host star. For transiting exoplanets three fundamental atmospheric measurements are possible: transmission spectra – where atmospheric absorption features are detected across an exoplanet's limb during transit, emission spectra – where the day-side average emission of the planet is detected during secondary eclipse events, and phase curves – where the spectral emission of the planet is mapped globally following the planet around its orbit. All of these techniques have been well proven to provide detailed characterisation information about planets ranging from super-Earth to Jupiter size. In this chapter, I present the overall background, history and methodology of these measurements. A few of the major science related questions are also discussed, which range from broad questions about planet formation and migration, to detailed atmospheric physics questions about how a planet's atmosphere responds under extreme conditions. I also discuss the analysis methods and light-curve fitting techniques that have been developed to help reach the extreme spectrophotometric accuracies needed, and how to derive reliable error estimates despite limiting systematic errors. As a transmission spectra derived from primary transit is a unique measurement outside of our solar system, I discuss its physical interpretation and the underlying degeneracies associated with the measurement.

David K. Sing
Astrophysics Group, School of Physics, University of Exeter, Stocker Road, Exeter, EX4 4QL,
UK, e-mail: sing@astro.ex.ac.uk

1 Background and History of Exoplanet Atmosphere Observations

Transiting planets are those that pass directly in front of their parent star as viewed from the Earth. During these events, the planet will block out a proportion of the starlight, which can be detected by time-series photometry. To be viewed in this privileged geometry directly passing in front (or behind) its parent star, transiting planets require a fortuitous orbital alignment with the Earth. As such, transiting exoplanets represent only a small fraction of the total exoplanet population. However, the fundamental properties such as the planetary mass and radius which can be determined (in many cases nearly free from astrophysical assumptions), and the detailed spectroscopic information that can also be measured make transiting exoplanets extremely valuable.

The planet-to-star radius ratio can be very precisely measured during a transit event, as the fractional flux deficit measured from a light curve, $\frac{\Delta f}{f}$, which is proportional to the projected area between the planet and star,

$$\frac{\Delta f}{f} \simeq \left(\frac{R_{pl}}{R_{star}} \right)^2, \quad (1)$$

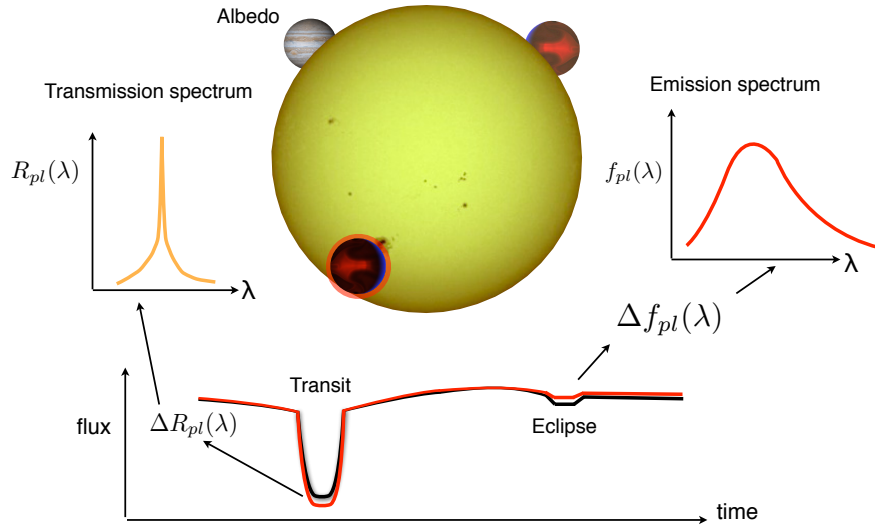


Fig. 1 Geometry of an exoplanet transit and eclipse event (top middle). During the exoplanet's orbit, the light curve of the system is monitored, with the transit and eclipse events detected from a drop in flux (bottom). A transmission spectrum is measured by detecting a change in transit depth as a function of wavelength (top left). A thermal emission spectrum is measured by detecting a change in the eclipse depth as a function of wavelength in the infrared (top right). The fraction of reflected light from the planet (the albedo) can be measured by observing the secondary eclipse at optical wavelengths.

where R_{pl} and R_{star} are the planet and stellar radii respectively. Stellar limb darkening also further modifies the transit light curve shape. As the radii of stars can generally be well determined, the radius of an exoplanet can be measured. Other fundamental properties of the exoplanetary system can also be derived from a transit's light-curve including the planet's inclination, the semi-major axis of the orbit, and the stellar density.

For planetary characterisation, the atmosphere is accessible through the transmission spectrum. When a planet passes in front of its host star, some of the starlight will be filtered through the atmosphere at the planet's terminator and will leave a spectral imprint. Atoms and molecules in the atmosphere will absorb and scatter light at characteristic frequencies, which will make the atmosphere at those wavelengths opaque at higher altitudes. In other words, the atmosphere will be optically thick in slant transit geometry higher in the atmosphere. The exoplanet will therefore have a slightly larger apparent radius at those characteristic wavelengths, which is directly observable via a deeper transit depth (see Fig. 1). In a sense, a transmission spectrum is essentially an absorption spectrum, as identification of atomic and molecular species in the planet's atmosphere are identified via absorbed stellar light, though a technically more accurate description is a transit radius spectrum. Exoplanet transmission spectra are now typically constructed by taking time-series spectrophotometry during a transit event, with the spectra divided into many wavelength bins in which the chromatic change in transit depth is measured. At each wavelength bin, a transit light curve must be fit with a model (typically including instrumental systematic effects along with a limb-darkened theoretical transit model) and the planet radius at a particular wavelength, $R_{pl}(\lambda)$, is extracted. A transmission spectrum is very sensitive to the atmospheric composition, which is typically among the first bits of information one learns when a positive signature is identified.

A planet's atmosphere can also be characterised from an emission spectrum. During secondary eclipse, when the planet is seen to pass behind its host star, the flux contribution from the planet drops to zero, isolating the flux from the star. Thus, the light from the planet can be efficiently separated from that of the star. The eclipse depth measured from the fractional flux deficit at secondary eclipse is directly proportional to the planet-to-star flux ratio, F_{pl}/F_{star} with,

$$\frac{\Delta f}{f} = \frac{F_{pl}}{F_{star}} \times \left(\frac{R_{pl}}{R_{star}} \right)^2. \quad (2)$$

Similarly to a transmission spectra, typically an emission spectra is constructed by taking time series spectrophotometry, and dividing the spectra into many different wavelength bins in which the eclipse depth is measured and the planet-to-star flux ratio is extracted. The amount of flux emitted by a planet at infrared wavelengths depends on its temperature, so this important planetary parameter can be measured with emission spectra in the infrared. Optical secondary eclipses are sensitive to the reflected light and the geometric albedo of an exoplanet.

Finally, when a planet is observed over the course of a full orbit, the flux contribution from the exoplanet will modulate the total star-plus-planet flux as its orbital

viewing geometry changes, with atmospheric information obtainable throughout the phase curve. While observing an exoplanetary phase curve does not require a transit or eclipse event, to date most phase curve studies have focused on transiting exoplanets as they typically offer better overall constraints. For instance, the total flux contribution to the phase curve from the star, which dominates the total signal, can only be precisely measured during a secondary eclipse event. From a phase curve, we can measure the day-to-night temperature contrast, which informs us about atmospheric recirculation. Additionally, the abundances of species and atmospheric temperatures can be mapped around the planet.

1.1 A Few Early Results

The following sections are by no means a complete summary or census of all exoplanet observations relating to atmospheric characterisation that have been obtained, nor is it meant to be. Further results can be found in several review articles (e.g. [Seager & Deming 2010](#); [Burrows 2014](#); [Bailey 2014](#); [Crossfield 2015](#); [Deming & Seager 2017](#)). The intention is to highlight a few representative works to give the reader a broad introductory overview of the types of atmospheric measurements that have and can be made regarding transiting exoplanets, and a flavour of the sort of scientific investigations that result.

1.2 Transit Observations

As recently as 2006 there were fewer than 10 transiting exoplanets known, and the atmospheric characterisation of these planets were largely limited to a few select cases. Among the first characterised planets was HD 209458b, a exoplanet first found using the radial velocity technique ([Mazeh et al., 2000](#)) which was the first planet discovered to also transit by [Charbonneau et al. \(2000\)](#) and [Henry et al. \(2000\)](#). Having initially been discovered by the radial velocity technique helped make HD 209458b particularly well suited for followup atmospheric characterisation. The radial velocity method requires bright target host stars in order to obtain sufficient signal-to-noise at high spectral resolution, which has historically limited radial velocity discoveries on moderately sized telescopes to V-magnitudes typically brighter than about 10. Transiting around such bright host stars opens up the possibility to perform very high precision photometry, as sufficiently large numbers of photons can be gathered during the short \sim hour long transit durations. Shortly after the discovery of transits, the Hubble Space Telescope (HST) observed HD 209458b during four transits with the Space Telescope Imaging Spectrograph (STIS). The resulting transit light curve ([Brown et al., 2001](#)) was unprecedented in quality with 110 parts-per-million photometric accuracies with an 80 second cadence. The high quality demonstrated not only the feasibility to perform atmospheric studies but also

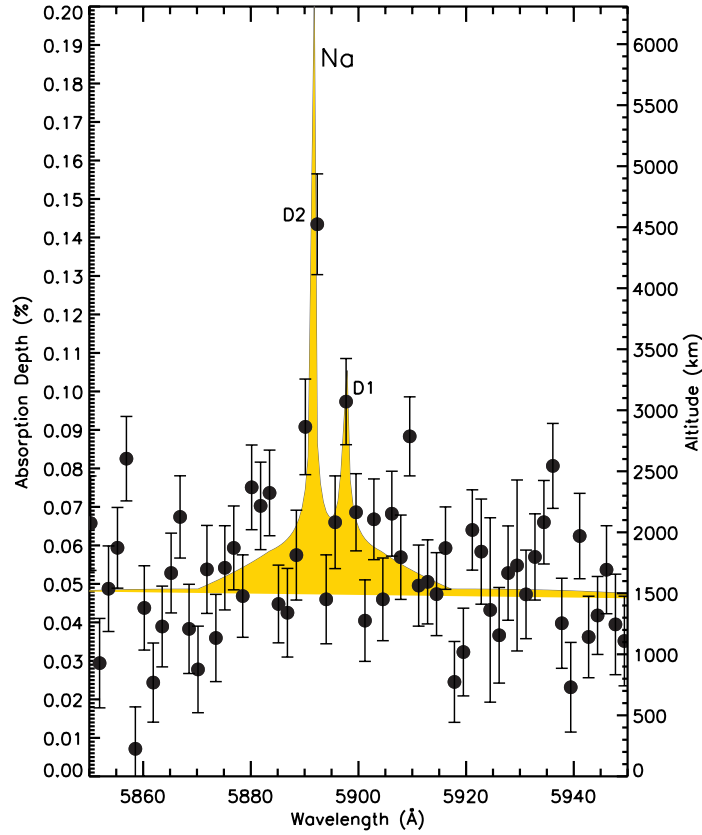


Fig. 2 Hubble Space Telescope transmission spectrum of HD 209458b showing sodium absorption, which was first detected by [Charbonneau et al. \(2002\)](#). Shown is the transmission spectrum adapted from [Sing et al. \(2008\)](#), which resolves the sodium doublet. The relative transit absorption depth and relative altitude in the planetary atmosphere are both indicated.

to detect Earth-sized exoplanets in transit around Sun-like stars (the NASA Kepler mission was selected 12 months later). With the same STIS data, [Charbonneau et al. \(2002\)](#) made the very first detection of an exoplanet atmosphere by observing excess absorption in the Na doublet (See Fig. 2). Alkali metal absorption had been previously predicted to be present in the atmosphere by [Seager & Sasselov \(2000\)](#), as the high temperature allows atomic sodium to exist in the gas phase.

The HD 209458b sodium detection was a good early indication of the high photometric precisions which would be needed to regularly make exoplanet atmosphere detections, as the observed sodium signal measured by [Charbonneau et al. \(2002\)](#) represented a deeper transit by just 232 parts-per-million (ppm) relative to the adjacent wavelengths and precisions of 57 ppm were needed to secure a 4- σ confident detection.

As the transit technique is reliant upon the starlight to make a measurement, and not light from the planet itself, a transmission spectrum can be studied across a much broader wavelength range than traditionally possible when observing only emitted radiation. Shortly after the sodium detection, HST STIS followed HD 209458b up again but this time in the far-ultraviolet (FUV), targeting the H I Ly- α line. An extended exosphere of H I was expected around the exoplanet, which could in principle be detected against the stellar chromospheric Ly-alpha emission during a transit event. However, the resulting transit depth as observed in H I (15%, [Vidal-Madjar et al. 2003](#)) was far in excess of the planet itself or even its Roche lobe, indicating hydrogen atoms are vigorously escaping from the planet. Oxygen and carbon were also detected in the exosphere by STIS shortly thereafter ([Vidal-Madjar et al., 2004](#)). With the second transiting planet discovered in 2003 ([Konacki et al., 2003](#)), for a short time, the number of atmospheric detections made via the transit method outpaced the number of transiting planets. Even with thousands of transiting planets known today, HD 209458b still resides as one of the very best theoretical targets for atmospheric characterisation.

Transmission spectral observations from the ground also proved feasible, first at high resolution. [Redfield et al. \(2008\)](#) observed HD 189733b across optical wavelengths with the Hobby-Eberly Telescope at high resolution (spectral resolution, $R \sim 60,000$). Significant absorption was detected in-transit in the Na D lines, indicating deeper transit depths by 672 ± 207 ppm. Similarly, [Snellen et al. \(2008\)](#) analysed optical HD 209458b transit data from the Subaru telescope at high resolution ($R \sim 45,000$). A significant non-linearity in the CCD had to be corrected, and once applied significant Na absorption was also detected (1350 ± 170 ppm). The Na absorption from HD 209458b first observed with Hubble was not only confirmed, but the Na line profile itself also matched well between the observations ([Charbonneau et al. 2002](#); [Sing et al. 2008](#); [Snellen et al. 2008](#)). Historically, such agreement between observations has not always been the case, but these early results did prove to place exoplanet atmospheric observations on a solid foundation.

The shape of absorption line profiles in transmission spectra can be used to probe different altitudes of exoplanet atmospheres. The wings of a line have a lower optical depth, and probe lower, cooler parts of the atmosphere, while the extended core of the line probes out to much higher altitudes. Because the atomic Na D resonance lines are very strong and have little other absorbers obscuring the view in their wavelength region, they are ideal for probing a wide altitude-pressure range. Their line profiles have been well-measured from HST and the ground for HD 189733b and HD 209458b (see also [Huitson et al. 2012](#); [Jensen et al. 2011](#)). Thermosphere layers were detected in both planets (e.g. [Vidal-Madjar et al. 2011](#) for HD 209458b and [Huitson et al. 2012](#) for HD 189733b). The thermosphere is an extended region above the typical lower layers of the atmosphere (troposphere and stratosphere), but below the exosphere, where UV radiation is absorbed and temperatures rise as a function of height. The cores of the Na lines extend to higher altitudes in the presence of a thermosphere, as the hotter thermospheric temperatures increase the pressure scale height and puff up the atmosphere - leading to larger transmission spectral features. For instance, HARPS observations of HD 189733b have resolved

the Na lines up to an altitude of 12,700 km (Wyttenbach et al., 2015). With high enough signal-to-noise (S/N), a change in pressure scale height at different altitudes can be directly detected, which then informs us about the temperature change in the atmosphere between the upper and lower layers (see section 4 below).

1.3 Eclipse Observations

In August of 2004 the HST STIS instrument failed, preventing further observations until a repair could be made. However, a year earlier the Spitzer Space Telescope was launched, and while it was not designed for exoplanet transit observations, the first secondary eclipse measurements were achieved shortly after in 2005 by Deming et al. (2005) for HD 209458b, while Charbonneau et al. (2005) targeted TrES-1b. As Spitzer is an infrared telescope, it is sensitive to the longer wavelengths needed to probe a hot exoplanet closer to its ~ 1000 K black-body emission peak. Additionally, at these longer wavelengths the parent star is significantly fainter, which further increases the contrast. Both exoplanets were observed to have secondary eclipse depths near 0.25% and from these single eclipse measurements, brightness temperatures (which assumes the planet emits as a black body) could be derived. The timing of the secondary eclipse measurements placed informative constraints on the orbital eccentricity. With these results, Spitzer in effect took the reins over a period of a few years as the leading (and virtually only) exoplanet characterising instrument. The repair of HST and installation of the WFC3 instrument in 2009 also enabled high-precision secondary eclipse measurements (e.g. Fig. 3).

With multiple secondary eclipse measurements at different wavelengths, Spitzer was able to build up the first rough broadband emission spectra, which could be compared to theoretical atmospheric models. An early result came from Knutson et al. (2008) who used Spitzer to build up a spectrum from five photometric channels between 3 and 30 microns for HD 209458b. These broadband spectra are very low resolution ($R \sim 5$ to 10), thus no specific molecular features can be resolved, though in principle very large-scale differences between atmospheric models are detectable. The HD 209458b measurements indicated the presence of a stratosphere where the temperature is seen to rise (rather than fall) at higher altitudes. Rising temperatures create conditions where hot atmospheric gas lies above cooler gas, which gives rise to spectral emission features. If a planetary atmosphere has a temperature-pressure (T-P) profile which only cools off with higher altitudes, only spectral absorption signatures from the overlying cooler gas could be observed. For HD 209458b, Knutson et al. (2008) found the wavelengths between 4 and 10 microns were significantly higher than would be expected from non-inverted T-P profiles which indicated H_2O was in emission (also see Burrows et al. 2007). While these specific measurements did not generally hold up to further scrutiny (see section 2.2 below), they were a strong motivation into further sophisticated theoretical investigations of the atmospheric dynamics and chemistry of highly-irradiated gas giant planets, and the first steps towards constraining such models with eclipse observations.

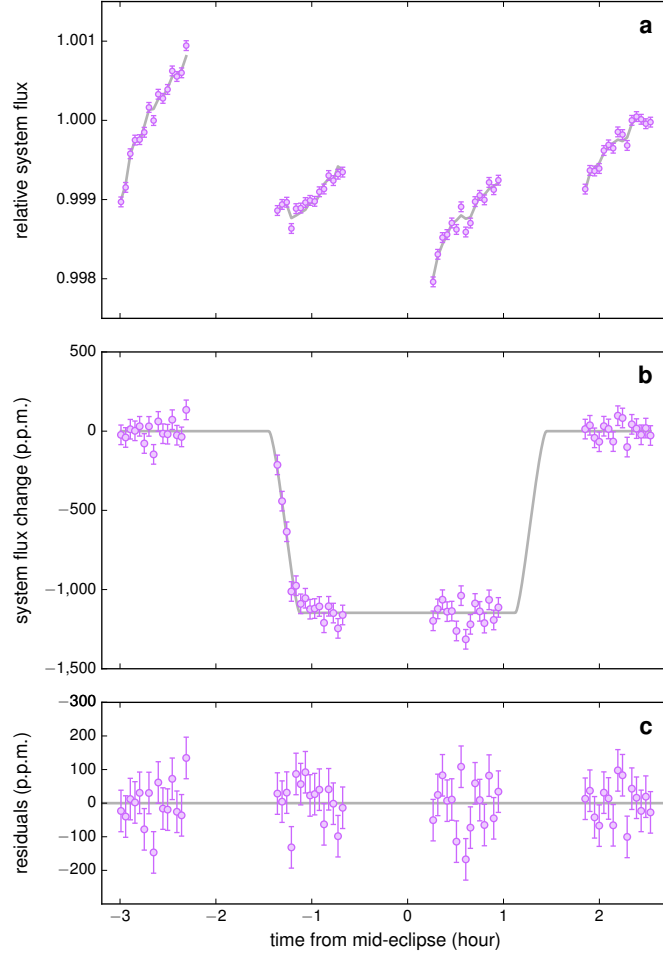


Fig. 3 Example of a secondary eclipse observation of WASP-121b from the Hubble Space Telescope WFC3 (from [Evans et al. 2017](#)). Plotted (a) is the raw normalized flux with photon noise error bars and the best-fit eclipse and instrument systematic trend model, (b) the relative change in system flux after correcting for instrument systematics, and (c) the residuals between the data and best-fit model showing precisions of 64 parts-per-million.

Atmospheric windows in Earth’s own atmosphere also permit exoplanet transit and eclipse observations from the ground. However, the challenges are formidable as precision photometry (~ 100 ppm) must be preformed for several hours against strongly changing weather conditions and instrument instabilities. Furthermore, for eclipse observations the largest signals occur at longer wavelengths which are generally inaccessible due to telluric H_2O absorption. Thus, exoplanet eclipse observations have generally been performed in the z' , J, H, and K atmospheric windows. Theoretical predictions early on ([López-Morales & Seager, 2007](#)) predicted

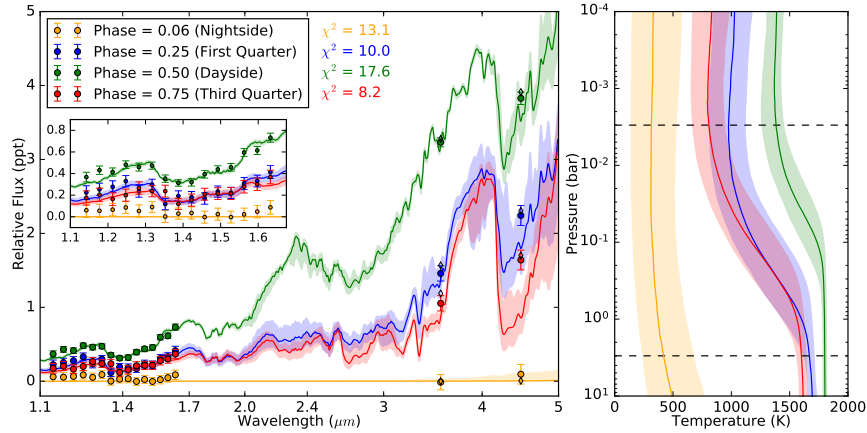


Fig. 4 Hubble Space Telescope WFC3 and Spitzer Space Telescope phase curve spectrum of WASP-43b at four different orbital phases (left) and the corresponding retrieved temperature-pressure profiles (right). Each set of colored circles depict measurements from the phase curve observations, and the colored curves with shaded regions represent the median models with 1σ uncertainties. The inset magnifies the WFC3 spectra. H_2O absorption is readily apparent in the spectra at 1.4 microns where a significant drop in the planet-to-star flux ratio is apparent. From [Stevenson et al. \(2017\)](#).

the hottest planets (~ 2500 K) would likely have significant and detectable thermal emission in the red-optical z' band, and shortly after [Sing & López-Morales \(2009\)](#) detected the thermal emission of Ogle-Tr-56b while at the same time [de Mooij & Snellen \(2009\)](#) detected the secondary eclipse of TrES-3b in the K band with the WHT telescope. These results directly demonstrated a very large number of exoplanet eclipses would eventually be observable, given that Ogle-Tr-56b orbits a very distant 16th magnitude star and the TrES-3b result was made with a modestly sized 4-meter telescope. [Croll et al. \(2011\)](#) observed eclipses of WASP-12b with the CFHT telescope at J, H, and K band which further demonstrated high-precision measurements could be obtained from the ground. Thus, exoplanet atmospheric characterisation from eclipses were no longer confined to flagship space telescopes, and transit and eclipse observations became demonstrably accessible for a wide range of targets using a wide variety of instrumentation.

1.4 Phase Curve Observations

In general, the most difficult atmospheric measurement to make with a transiting exoplanet is that of the phase curve. The difficulty stems from the requirement to maintain high photometric precisions of order 100 ppm (which, as with transits and eclipses, are still necessary) over long timespans. Typically, measurements last on the order of the orbital period of the planet, which can be a day or longer - compared

to transit/eclipse events which last a few hours. Furthermore, taking into account the very large telescope times needed, for practical purposes phase curve observations thus far have been focused on the shortest period planets with periods of 2 days or shorter.

While early non-continuous observational attempts were made (Harrington et al., 2006), a notable phase curve observation was made by Knutson et al. (2007b), who observed HD 189733b with the Spitzer Space Telescope at 8 microns during half an orbital period covering a transit and eclipse. The measured phase curve amplitude indicated a modest day-night circulation, which results in more modest phase curve amplitudes. In addition, the brightest portion of the phase curve was observed just before secondary eclipse. For a tidally locked planet, one may expect the hottest and thermally brightest point on the planet to occur at the sub-stellar point. However, strong atmospheric winds (as predicted by Showman & Guillot 2002) have the effect of advecting the heat and hottest part of the planet westward of the substellar point. Longitudes westward of the sub-stellar point are maximally viewable just before the secondary eclipse event itself, leading to an observed light curve where the maximum flux is found before an eclipse.

An important aspect of phase curve observations done on transiting planets is that a transmission spectrum and an eclipse spectrum can also be derived from the same dataset, making it a particularly constraining measurement. An example can be seen in Figure 4 where a spectroscopic phase curve of WASP-43 was observed by Stevenson et al. (2014, 2017) with HST and Spitzer. In the phase-curve spectra, H₂O features were mapped around the planet, and the emission spectrum showed strong absorption features.

1.5 Accessible Transmission Spectra Exoplanets

In 2006, there were 158 known exoplanets, with the majority of the population found from the radial velocity technique. Moreover, only a very small handful of exoplanets had their atmospheres regularly detected, most notably HD 209458b and HD 189733b. Not all exoplanets are ideal atmospheric targets. The more massive exoplanets have smaller atmospheric scale heights due to the high surface gravity, and will have smaller transmission spectral signals. For secondary eclipses, cooler exoplanets will have low thermal fluxes in the optical and near-IR, so will be more challenging to detect at those wavelengths.

For an exoplanet transmission spectrum, a good indication of the expected signal can be estimated by calculating the contrast in area between the annular region of the atmosphere observed during transit and that of the star. The characteristic length scale of the atmosphere is given by the pressure scale height,

$$H = \frac{k_B T}{\mu g} \quad (3)$$

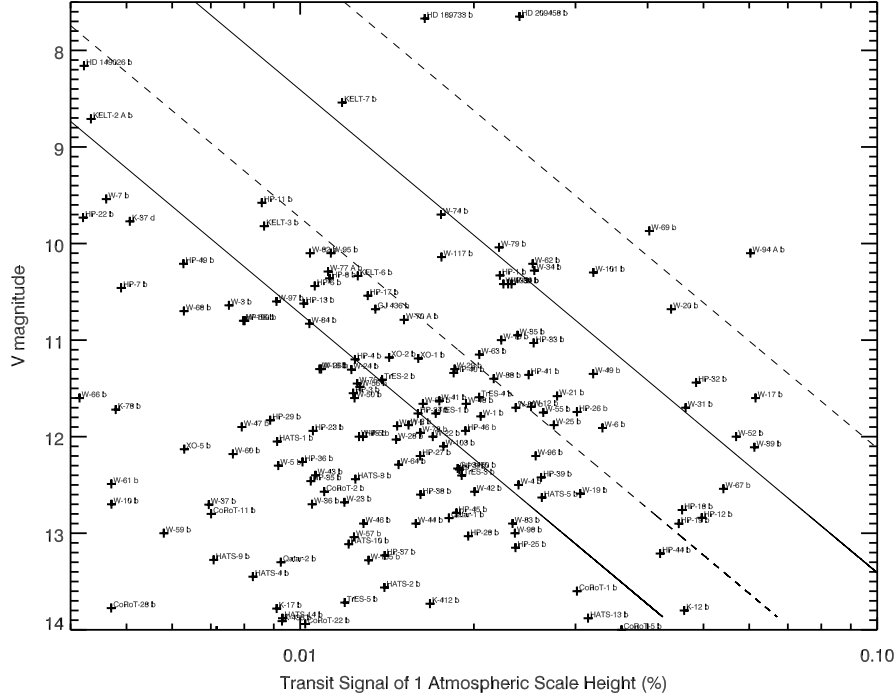


Fig. 5 Transmission spectral signal of 1 atmospheric scale height. Planets to the upper-right of the figure are easier to observe. The lines indicate approximately constant S/N values. The exoplanet data was compiled from the exoplanets.org database. The WASP and HAT-P planetary names have been abbreviated.

where k_B is the Boltzmann constant, T is the temperature of the atmosphere, μ is the mean mass of atmospheric particles, and g is the surface gravity. For giant exoplanets, the composition of the atmosphere can be assumed to be dominated by a H/He mixture of near-solar composition, which gives $\mu = 2.3 \times u$ where u is the unified atomic mass unit (Lecavelier des Etangs et al., 2008). For transiting exoplanets, the surface gravity is well known for a large majority of the prime transmission spectral targets, as historically the radial velocity method has been used to confirm the planetary nature of a transiting object. Those exoplanet systems too faint to be detected via radial velocity are also often too faint to perform detailed atmospheric characterisation. Moreover, knowing the mass of an exoplanet for transmission spectroscopy is vital, as large degeneracies will be present if the mass is unknown which will limit the usefulness in constraining the atmospheric properties.

A good way to estimate the atmospheric temperature is to use the equilibrium temperature value, T_{eq} . Assuming zero albedo and complete redistribution of heat around the planet, T_{eq} can be calculated using,

$$T_{eq} = (1/4)^{1/4} T_{eff} \sqrt{\frac{R_{star}}{a}} \quad (4)$$

where a is the semi-major axis of the planet and T_{eff} is the stellar effective temperature (Cowan & Agol, 2011). The temperatures derived thus far from transmission spectra have often been well within these equilibrium values. For example, HD 189733b, HAT-P-12b and WASP-6b have temperatures derived from their transmission spectra of 1340 ± 150 K, 1010 ± 80 K and 973 ± 144 K, respectively which compare very favourably to their T_{eq} values of 1200, 960, and 1150 K, respectively (Sing et al., 2016). With the scale height estimated, it is straightforward to approximate the absorption signal, A , of the annular area of one atmospheric scale height H during transit, as

$$A = \frac{(R_{pl} + H)^2}{R_{star}^2} - \left(\frac{R_{pl}}{R_{star}} \right)^2, \quad (5)$$

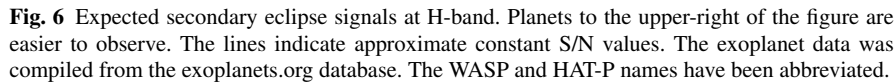
which can be further simplified assuming $H \ll R_{pl}$ to,

$$A = \frac{2R_{pl}H}{R_{star}^2}. \quad (6)$$

Transmission spectral signals are typically on the order of 1 to $\sim 5H$ in size, thus if the transit depth can be measured to about $1H$ in precision with sufficient spectral resolution, detectable spectral features would begin to appear. Plotting A against the magnitude of the host stars is a good proxy to compare the relative signal-to-noise of different exoplanets. While other factors such as cloud cover will ultimately determine if atmospheric features will be present or not, all other factors being equal, it is often a good guide to prioritise exoplanets with the largest expected signal-to-noise values. From Figure 5, the prominence of HD 189733b and HD 209458b become apparent. Both exoplanets orbit much brighter stars ($V \sim 7.7$) than the bulk of the known transiting planets, which dramatically improves the photon noise limits. The ‘‘puffiest’’ planets, like WASP-17b may orbit a much fainter star ($V=11.6$) but the expected atmospheric transit signal is large ($A \sim 0.06\%$) making it a comparable target to HD 189733b in terms of expected S/N. Perhaps 100 or more transiting exoplanets are now accessible with today’s instruments. In practice, other practical considerations are necessary to take into account. For instance, ground-based multi-object spectroscopy requires reference stars to perform differential spectrophotometric measurements. However, few, if any suitable reference stars would likely be available for observing a 7th magnitude target with a typical 4 to 8 metre class telescope. Such instruments have typical fields of view of around 10 arc minutes, and it is unlikely that more than one bright (and hence nearby) star would be close to each other in the sky.

1.6 Exoplanets With Accessible Secondary Eclipses

Not all exoplanets are favourable for secondary eclipse measurements. The expected eclipse depths can be estimated in a similar exercise as for transmission spectra. However, the results will be much more dependant on the observed wavelength,


$$\frac{\Delta f_{day}}{f} = p_{\lambda} \left(\frac{R_{pl}}{a} \right)^2 + \frac{B_{\lambda}(T_{day})}{B_{\lambda}(T_{eff})} \times \left(\frac{R_{pl}}{R_{star}} \right)^2, \quad (7)$$

which takes into account a reflection component with the wavelength dependant albedo p_λ , and a thermal component B_λ which is approximated here assuming the planet radiates as black body with temperature T_{day} , and the star also radiates as a black body with temperature T_{eff} (Haswell, 2010). Similarly to Figure 5, the expected secondary eclipse depth at a given wavelength can then be plotted against the host star magnitude, at that wavelength range, to assess the relative observability of different targets. Of course, in reality stars are not blackbodies, and neither are planetary atmospheres so there can be significant deviations from such simple estimations. Nevertheless, such plots as shown in Figure 6, can help illustrate the relative potential signal sizes between planets, all else being equal.

1.7 Accessing the Atmospheres of Small Exoplanets

Since the transit technique is predominately limited by the flux of the host star, it can be used across a much broader wavelength range than secondary eclipse measurements. Transits have been measured in the UV (e.g. [Vidal-Madjar et al. 2003](#)) through to the far-infrared ([Richardson et al. 2006](#)). Additionally, much smaller exoplanets are currently accessible with transit spectroscopy than with other techniques. There is strong interest to push characterisation down to smaller, cooler planets and so toward potentially life bearing worlds. The task is difficult, as small planets and cooler temperatures result in much smaller transit atmospheric signatures (see [Fig. 7](#)). To overcome this difficulty, currently there are two strategies being pursued to meet the near-term goal of detecting atmospheric features and viably searching for biomarker signatures within the atmospheres of extrasolar planets; transit spectroscopy of exoplanets around small M-dwarfs (the 'M-dwarf opportunity') or around very bright stars (the 'bright-star opportunity'). These opportunities have driven dedicated transiting M-dwarf searches, such as MEarth ([Charbonneau et al., 2009](#)), as well as dedicated space missions such as TESS and PLATO which will search the brightest stars for transits.

While searching for signatures of habitability will be an important long-term exoplanet goal, it must be put into perspective as the very wide and diverse group warm-Neptunes, super-Earths and small terrestrial exoplanets represent a completely uncharted parameter space. Developing a comprehensive theory to explain the atmospheres of these planets more generally, and therefore put any atmospheric detection within a wider context will represent an enormous challenge.

The discovery of the super-Earth GJ1214b orbiting an M-dwarf ([Charbonneau et al., 2009](#)) provided the first atmospheric glimpses into small exoplanets ([Bean et al., 2010](#)). GJ1214b orbits a small, M4.5 dwarf star, which means it has a large transit depth and atmospheric transmission signal. Both of these observable quantities scale inversely with the radius of the star squared, so the signals of exoplanets orbiting smaller stars are greatly enhanced. For GJ1214b, the star has a radius of $R_{star}=0.2 R_{\odot}$ making an exoplanet signal $(1/0.2)^2=25\times$ higher than if the same planet orbited a sun-like star. The discovery of TRAPPIST-1b,c,d,e,f,g ([Gillon et al., 2017](#)) has pushed the M-dwarf opportunity to even smaller planets and stars, with the $0.114 R_{\odot}$ sized M8 star providing transmission spectral signals $77\times$ higher than if the same planet orbited a sun-like star. To this end, even the atmosphere of Trappist-1f, which is an Earth-sized exoplanet orbiting within the habitable zone and is expected to be rocky, may potentially be detected in the near-future. Even with a large signal boost from a small star, the atmospheric features are still expected to be small and challenging to detect. Current facilities such as HST have allowed H-dominated atmospheres to be ruled out on several of the TRAPPIST-1 planets ([de Wit et al., 2016](#)).

On the bright end, the discovery of a planet transiting around HD 97658b ([Dragomir et al., 2013](#)) permitted atmospheric investigations of a super-Earth around a much more massive K1V star. In both the case of HD 97658b and GJ1214b, the

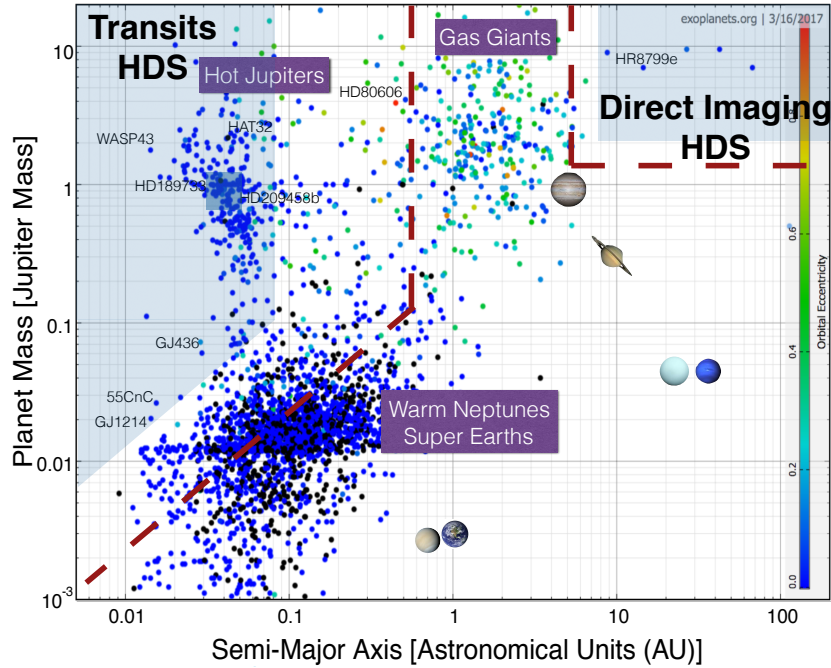


Fig. 7 Planet Mass vs. Semi-Major Axis for the detected exoplanets, compiled from the exoplanets.org database. The broad exoplanet types are labeled and solar system planets also indicated. The approximate current sensitivity of atmospheric studies is indicated (dark shaded region) and near-term expected improvements (red dashed lines).

exoplanet's atmospheres proved to be largely consistent with heavy cloud-cover and no spectral features were detected (Knutson et al., 2014; Kreidberg et al., 2014b).

2 Exoplanet Atmosphere Science Topics

In the following sections, I have highlighted a few current science topics which transiting exoplanet atmosphere observations can (or will hopefully) address. While there are a very wide and diverse range of science topics, many fall under a few basic categories which are briefly described below.

2.1 Planet formation

Gas giant exoplanets are predominantly composed of a H/He mixture, which was accreted during the planets formation from the protoplanetary disk. As such, the

gas is primordial in nature so may be expected to contain records of the formation conditions in which the planet formed. As transiting exoplanets are amenable to spectroscopic studies, one may expect then to probe what would be essentially the primordial gas and gain insights into the planet formation process.

There are two widely considered theories for how gas giant planets form: gravitational instability and core accretion. Gravitational instability is said to occur when the protoplanetary disk rapidly cools and collapses into planetary-mass fragments (Boss, 1997). Planets formed via this mechanism would have the same bulk compositions as their local protoplanetary disk material and their host stars. Alternatively, in the core-accretion model, giant planets form in a multi-step process: first, sticky collisions of planetesimals lead to the formation of protoplanetary cores; then, once the cores reach a threshold mass they accrete nearby gas in a runaway fashion (Pollack et al., 1996). Population synthesis models from Mordasini et al. (2012) and Fortney et al. (2013) suggest that in the core accretion paradigm, as the mass of a planet decreases, its atmospheric metallicity increases. This is because lower mass planets would be unable to accrete substantial gas envelopes, and thus would be more susceptible to pollution by in falling, higher metallicity planetesimals. The giant solar system planets agree with the latter scenario (see Fig. 8), as the metallicities derived from the methane abundance of Jupiter (from the Galileo probe: Wong et al. 2004), Saturn, Neptune, and Uranus (from infrared spectroscopy: Fletcher et al. 2009; Karkoschka & Tomasko 2011; Sromovsky et al. 2011, respectively) show decreasing metal enhancement with increasing planet mass. Via these two theories, exoplanetary atmospheres will exhibit different atmospheric properties which can be measured from transmission and emission spectroscopy. Gravitational instability theory suggests that planets will have the same atmospheric metallicity as the central star, while in core accretion theory lower mass planets will have higher atmospheric metallicity.

Gas-giant exoplanets are widely expected to have retained the bulk of their primordial atmospheres, and measuring the atmospheric abundances across a wide range of planet masses should provide insight into formation mechanisms. Kreidberg et al. (2014a) found evidence the $2M_J$ hot Jupiter WASP-43b follows the same inverse mass-metallicity relationship as the solar system planets. However, the Neptune-mass exoplanet HAT-P-26b has a measured water abundance at just $4\times$ solar (Wakeford et al., 2017) which is below the trend and suggests a different formation and/or evolutionary processes. HAT-P-26b is consistent with recent envelope accretion models (Lee & Chiang, 2016), which argue that most hot Neptunes accrete their envelopes in situ shortly before their disks dissipate. In both studies, the retrieved atmospheric water abundance was used as a proxy for the overall planet's metallicity but the abundant carbon-bearing molecules will need to be measured before stringent metallicity constraints are available.

The abundance ratio between carbon-bearing molecules and oxygen-bearing molecules (C/O) is also expected to play a key role in constraining planet formation and migration mechanisms (Madhusudhan et al., 2014). The C/O ratio contains vital information such as the physical properties of the accretion disk in which the planet formed, and a planets location within that disk. This is especially pertinent

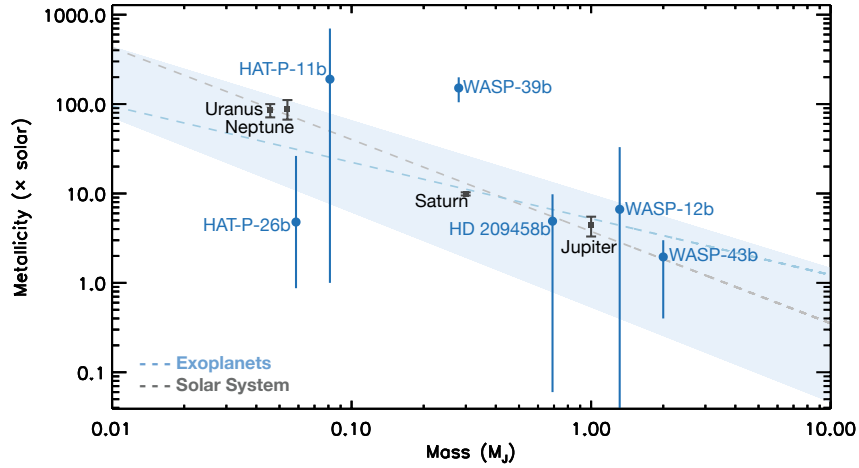


Fig. 8 Mass-Metallicity trend for solar system planets and exoplanets, adapted from Wakeford et al. (2017) to include measurements of WASP-39b (Wakeford et al., 2018), and HD 209458b (Line et al., 2016).

for hot Jupiters, which migrated to short orbital periods though may have initially formed beyond the snow line (e.g. Öberg et al. 2011). Carbon-rich atmospheres would point to scenarios where hot Jupiters were initially located beyond the snow line and accreted primarily carbon-rich gas, while O-rich atmospheres would point instead to accretion of primarily oxygen-rich solid material (Espinoza et al., 2017).

2.2 Atmospheric Physics

Transiting exoplanets represent a new novel laboratory in which to test our models of atmospheric physics. The temperatures, gravities, and chemical compositions occupy a very wide and new range of physical conditions, making observations of these planets capable of giving new broad physical insights into how planetary atmospheres operate. Current theories of hot gaseous planets contain many open questions about their atmospheric characteristics (temperature, clouds, energy budget, atmospheric escape), their chemical abundances, and how they formed and evolved. All these questions are intertwined, and by observing, characterising, and comparing many exoplanets across a broad parameter space, progress on answering some of those questions can be made.

Transiting planets orbit close to their host stars, making them tidally locked and highly irradiated. Those factors affect the planet's vertical and horizontal (day-to-night) temperature structure, and induce photochemical processes in their atmospheres, which do not occur in the most related astrophysical objects, isolated brown

dwarfs (BD). Therefore, hot exoplanets are completely new objects with a set of physical processes that are uniquely challenging to theoretically model.

From the first observations of secondary eclipse spectra, the thermal structure of hot Jupiters has been an active area of theoretical investigations and observational efforts. One of the first planets characterized through secondary eclipse measurements showed evidence for a thermal inversion and hot stratospheric layer (Knutson et al., 2008). A hot stratosphere is caused by strong optical absorbers, which absorb stellar radiation at altitudes higher than they thermally radiate energy, which heats the upper atmosphere and causes a stratospheric layer (Hubeny et al., 2003; Burrows et al., 2007; Fortney et al., 2008). On the Earth, UV absorption by ozone creates a stratospheric layer and most solar system planets including Jupiter and Saturn have stratospheres (Gillett et al., 1969; Wallace et al., 1974; Ridgway, 1974).

The presence or absence of a stratosphere is expected to change the global energy budget and atmospheric circulation and dynamics of the planet, making their presence and theoretical understanding an important aspect of their overall atmospheric makeup. In highly irradiated gas giant exoplanets that lack a strong optical absorber, the incident stellar irradiation is absorbed deep in the atmosphere, near pressures of 1 bar (see Burrows et al. 2008). This pressure is close to the near-IR emission photosphere, resulting in a monotonically decreasing temperature profiles and a lack of a stratosphere. At these pressures, the expected wind speeds in a hot Jupiter will be able to efficiently redistribute heat around the entire planet, leading to modest day/night temperature contrasts. With a strong optical absorber at high altitudes, the local gas is radiatively heated by the incident stellar flux, creating a stratosphere. In addition, the winds at these lower pressures (higher altitudes) are not able to efficiently redistribute the energy at their near-IR photospheres, creating a very strong day-night temperature contrast. With a stratosphere, the hottest part of the planet becomes located at the highly irradiated sub-stellar point, while the atmosphere becomes cooler towards the limb.

Several candidates for strong optical absorbers at altitude were proposed (Hubeny et al., 2003; Burrows et al., 2007; Fortney et al., 2008) with TiO/VO being the currently leading candidates. Fortney et al. (2008) highlighted the importance of gaseous TiO and VO to the optical opacities of highly irradiated hot-Jupiters, proposing two classes analogous to M and L-type dwarfs. In this scenario, hot-Jupiters warm enough to still have gaseous TiO and VO were dubbed pM Class planets. This class contains temperature inversions, and appears anomalously bright in the mid-infrared at secondary eclipse, as the stellar incident flux is absorbed high in the atmosphere and emitted as thermal flux at near-IR wavelengths. Theoretical models predicting the transmission spectra of pM class of planets would be dominated in the optical by TiO opacity (Fortney et al., 2008). The optical transmission spectra of cooler pL Class planets (lacking TiO) are thought to be dominated by neutral atomic Na and K absorption, and lack hot stratospheres.

Follow-up studies of HD 209458b with more advanced data analysis techniques did not support the presence of a stratosphere (Diamond-Lowe et al., 2014; Evans et al., 2015). In addition, despite many dozens of exoplanets searched for signatures of stratospheres with Spitzer, no definitive detections were made and confirmed. For

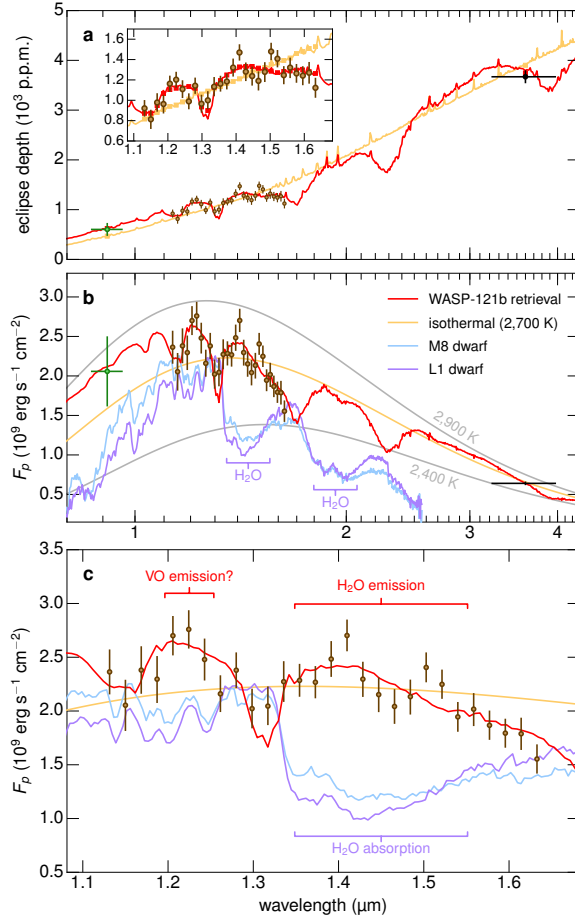


Fig. 9 Emission spectrum of WASP-121b from [Evans et al. \(2017\)](#). Shown is the measured HST, Spitzer, and ground-based eclipse depths and the $1\text{-}\sigma$ uncertainties, the horizontal error indicate the photometric bandpasses. The yellow lines show the best-fit isothermal blackbody spectrum with a temperature of 2,700 K, while the red lines show the best-fit atmospheric model from a retrieval analysis. The middle and lower panels show isolated planetary flux with the stellar contribution removed, and observed spectra for a M8 and L1 dwarf are shown for comparison (blue and purple lines), exhibiting H_2O absorption bands. For WASP-121b the H_2O band appears in emission. Spectra for 2,400 K and 2,900 K blackbodies (grey lines) indicate the approximate temperature range probed by the data.

a while it seemed TiO/VO may not be present in hot-Jupiter atmospheres. [Spiegel et al. \(2009\)](#) argued that vanadium oxide was not likely to fulfil this role due to low abundances, and that the previously favoured titanium oxide would require unusually high levels of macroscopic mixing to remain in the upper atmosphere.

A decade later, the topic of hot Jupiter stratospheres is still a hot topic as a thermally inverted spectral signature was observed for WASP-121b with H_2O seen in emission (see Fig. 9 and [Evans et al. 2017](#)), and evidence for a stratosphere and TiO seen in WASP-33b as well ([Haynes et al., 2015](#); [Nugroho et al., 2017](#)). Compared to earlier studies, WASP-121b and WASP-33b are much hotter ($T_{\text{eq}} > 2500\text{ K}$) than the planets probed earlier, which could indicate much hotter temperatures are required than earlier theoretical studies indicated ([Fortney et al., 2008](#)). However, it remains unclear why some planets would have stratosphere layers, while other seemingly similar very hot planets do not.

2.3 Clouds and Hazes

Cloud and haze aerosols are ubiquitous for the planets with significant atmospheres within our own solar system. For hot exoplanets currently amenable to transit characterization, clouds and hazes have also been found. The atmospheric temperatures of the hot Jupiters are close to the condensation temperatures of several abundant components, including silicates and iron. The formation of condensate clouds and hazes is a natural outcome of chemistry in much the same way H, C, and O combines to form H_2O , CO, and CH_4 . The possible presence of such condensation clouds was considered early on (Seager & Sasselov, 2000). Cloud and haze aerosols can form via condensation chemistry, or alternatively the aerosols may be photochemical in nature (e.g. Helling et al. 2008; Marley et al. 2013). Silicate and high-temperature cloud condensates are expected to dominate the hotter atmospheres, while in cooler atmospheres sulphur-bearing compounds are expected (Visscher et al., 2010; Morley et al., 2012; Wakeford & Sing, 2015). The presence or absence of clouds and hazes have strong implications on all aspects of a planet's atmosphere including the radiation transport, chemistry, total energy budget, and advection (Marley et al., 2013). As such, the presence of clouds and capacity to model them is currently a major uncertainty and limitation in our ability to interpret exoplanet spectra and retrieve accurate molecular abundances.

According to models, condensates would weaken spectral features, or mask some of them, depending on the height of the cloud deck (Marley et al., 1999; Sudarsky et al., 2003; Fortney, 2005). In transmission spectra, a grey cloud (for example) can mask all absorption features below the altitude of the cloud deck, and is an explanation for the muted water feature of HD 209458b (Deming et al., 2013) and the absence of features on the super-Earth GJ1214b (Kreidberg et al., 2014b). The HST transmission spectrum of HD 189733b was found to contain a high altitude scattering haze (Pont et al., 2008), which has since been confirmed by multiple follow-up HST measurements (Sing et al., 2011; Huitson et al., 2012; Gibson et al., 2012b; Pont et al., 2013). For HD 189733b, the haze covers the entire optical regime, with a Rayleigh scattering slope masking all but the strong Na I line cores and likely extends into the near-IR, covering or muting the water absorption features (see Fig. 10). Most of the exoplanets characterized thus-far show some levels of clouds (Sing et al., 2016), though the strong diversity of cloud and haze covers found thus far indicates there will be a sizeable population hot Jupiters with largely clear atmospheres, especially in the infrared where the scattering opacity of hazes and clouds is likely to become greatly reduced.

3 Analysing Transmission Spectral Data

In the following sections, some of the basic data analysis procedures that have been developed to handle transit and eclipse spectrophotometry at high precision are reviewed. Included is a broad overview of the reduction steps, time series fitting meth-

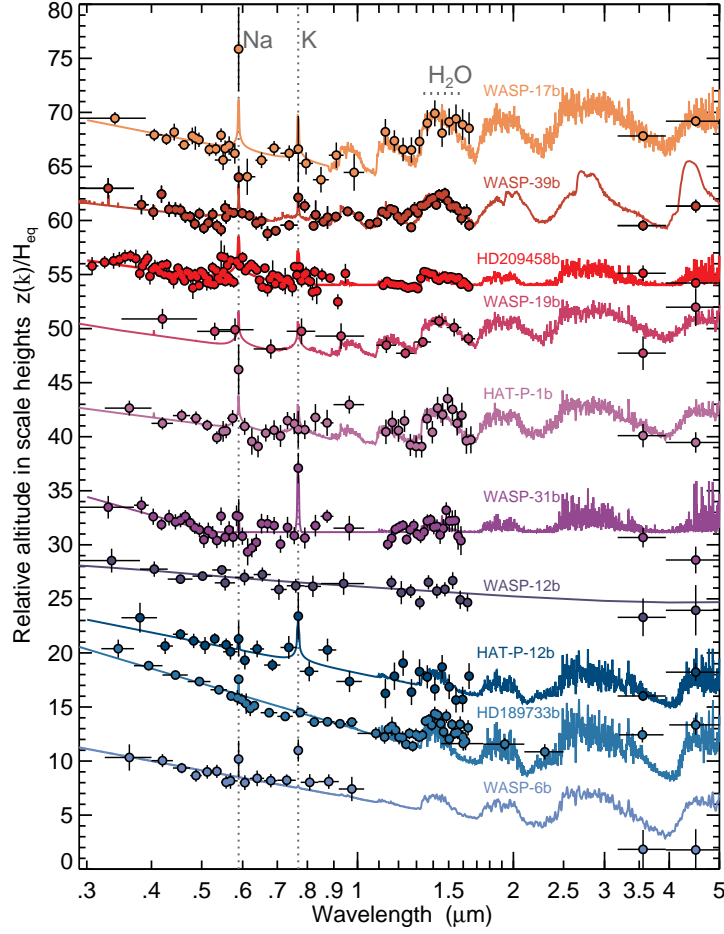


Fig. 10 Adapted from [Sing et al. \(2016\)](#). Shown is the HST/Spitzer transmission spectral sequence of hot-Jupiter survey targets, with data from [Wakeford et al. \(2018\)](#) for WASP-39b also included. Solid coloured lines show fitted atmospheric models and the prominent spectral features including Na, K and H₂O are indicated. The horizontal and vertical error bars indicate the transmission spectra wavelength bin and 1σ uncertainties, respectively. Planets with predominantly clear atmospheres (towards top) show prominent alkali and H₂O absorption, with infrared radii values commensurate or higher than the optical altitudes. Heavily hazy and cloudy planets (towards bottom) have strong optical scattering slopes, narrow alkali lines and H₂O absorption that is partially or completely obscured.

ods, statistical tools, and methods to handle different noise sources. When pushing transiting exoplanet spectroscopy to very high (few ppm) levels, all potential sources of noise tend to matter, and even what may appear to be very minor effects can become important limiting factors.

3.1 *Pre-observation steps*

An important but often overlooked aspect of observational astronomy and transiting exoplanet characterization is the steps one has to make and plan for well in advance of working with any new dataset. Most all good science starts with an idea, and a science question to investigate. For transiting exoplanet science, even fifteen years after the first atmospheric detection there are still no dedicated instruments designed from the beginning to perform the difficult task of obtaining the 10's or even 100's of ppm level photometric precisions across hour-long timescales necessary. This is in stark contrast to a dedicated instrument such as HARPS, which has proven \sim m/s radial velocity accuracies can be reliably achieved. As such, the planing and executing of transit/eclipse data still requires special care. Space-based data remains the gold standard, as the data quality is much more homogenous and the levels of precision demonstrated are much more reliably obtained. Nevertheless, a common mistake often made is to be overly optimistic or unrealistic in the levels of precision that can be achieved, and the size of potential atmospheric signatures. The current history of transiting exoplanet atmospheres has shown that more often than not, the atmospheric signal sizes observed are smaller than predicted, and the noise levels achieved are usually larger than photon limited (which exposure time calculators assume). Such was the case for Na on HD 209458b ([Charbonneau et al., 2002](#)) which was about $3\times$ smaller than predicted, and most of the H₂O features seen by HST to date as well have also been considerably smaller than predicted (e.g. [Deming et al. 2013](#); [Wakeford et al. 2013](#); [Kreidberg et al. 2014b](#)). Such has the case been with secondary eclipse measurements as well, with the [Grillmair et al. \(2008\)](#) Spitzer spectrum of HD 189733b showing H₂O features which were much smaller than earlier models (e.g. [Burrows et al. 2008](#)). Much of the smaller features are likely due to natural explanations such as clouds and hazes, which are still not robustly handled by most theoretical forward models given the complexity. For an observer, these aspects need to be kept in mind when planing one's observations to ensure detections can be made even if photon noise is not achieved and the signals sought for are smaller than expected. After all, the end goal is (or should be) to obtain robust, impactful results published in reputable journals, not just to collect data.

Basic Pre-Data Procedure Steps:

1. Have great idea to solve important science question, linking it to potential observations.
2. Check to see if the appropriate observations can be acquired, and with sufficient S/N. Do not be overly optimistic or unrealistic in what can be achieved, if so, even if telescope time is awarded and good data is acquired, luck will be needed to obtain impactful results.
3. Write a great telescope proposal(s).
4. Submit the proposal & convince a skeptical allocation committee.
If rejected, revise proposal and resubmit next call if the case remains strong.
5. Plan the observations very carefully.

- a. Being paranoid of mistakes is often a good thing.
 - b. Execute the observations very carefully.
 - c. Do not underestimate the value of calibration frames.
 - d. Make use of your collaborator's expertise.
 - e. Maintain high photometric precisions over continuous multi-hour timescales.
Most telescope operators are not used to the methods to obtain high photometric precisions (e.g. no dithering due to the relative nature of the measurement) and care must be taken to ensure the observations are executed properly.
6. Download/collect images.

3.2 *Initial calibration overview*

After obtaining a time-series dataset, the first data-reduction steps are much the same as any other method. However, before one begins reducing data it is a very good idea to inspect each of the data-frames in detail. A time-series dataset may contain hundreds or perhaps thousands of images. With these large numbers, it can be easy to overlook subtle issues which may not be obvious after aperture photometry is performed or the spectral trace is extracted. Stretching an image and adjusting the image contrast to view the high and low count level features can reveal possible issues such as bad pixels, and making time-series movies of the data or blinking frames can be a good method to reveal and get a feel for potential issues such as positional drifts, cosmic rays, and detector ghosts. Unexpected features may appear as well, as very unlikely asteroid or satellite crossing events have been noticed in HST time series data.

For HST WFC3 data, time-series spectral pixel maps can be utilised where a 2D histogram of the count levels at each pixel in a spectra are plotted vs time (e.g. Fig 11). As positional drifts are a major cause of systematic errors in WFC3 spatially scanned data, these maps help reveal the extent of such drifts, and the presence of bad columns.

The first reduction steps with modern 2D image or spectral data are essentially the same as all other traditional areas of astronomy. For CCD data, the images are typically:

- Trimmed of overscan regions, leaving the areas of the chip that contain useful data.
- Individual bias frames are combined.
- The flat-fields and science frames are processed to remove the overscan and average bias.
- Bad pixel maps are constructed.
- Flat-field images are combined and normalized.

For time-series data, there is an important difference between low-frequency features (large scale trends) in a flat-field, and high-frequency pixel-to-pixel trends. A widely adopted method for most all time-series transit/eclipse data is to keep

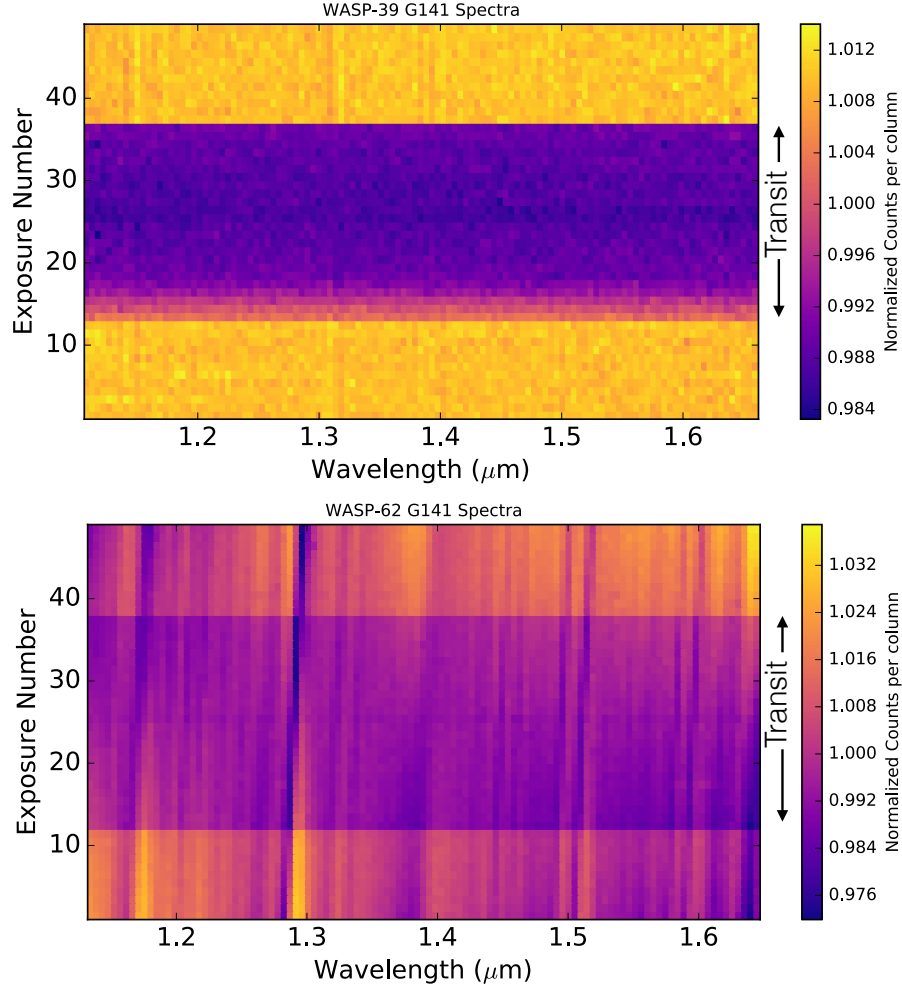


Fig. 11 Time-series spectral pixel maps for HST WFC3 G41 transit data of WASP-39b (top) and WASP-62b (bottom) used to visualise the overall data quality. Plotted is the normalized count level at each pixel in the spectra vs time during the transit observation. The transit event in both plots is evident by the drop in flux centred near the middle of both plots. The WASP-62b transit suffered from a guidestar problem which negatively impacted the telescope guiding, and large drifts on the order of several pixels can be seen. This problem negatively impacts the photometric quality of the spectroscopic channels, as is apparent by the systematic trends which drift in wavelength during the observation. An example of a good quality dataset is shown for WASP-39b (top) for comparison, which does not show such wavelength-dependent trends. Figs. courtesy of H. Wakeford.

the point-spread-function of the telescope on the same pixel (or sub-pixel if possible) during the entire course of the observations. By doing so, low-frequency flat-field features are not important and largely do not impact the photometry. A transit or eclipse light curve is a differential measurement, and the absolute gain

or count levels on the detector are not utilised as each light curve is individually normalized to the out-of-transit levels. Thus, many observers choose not to apply a flat-field correction, as it has been sometimes been seen to introduce noise (e.g. [Gibson et al. 2017](#)). A successful flat-field correction, however, can correct for high-frequency pixel-to-pixel variations. These smaller scale gain differences between neighbouring pixels can become important if the telescope pointing is not entirely stable during the night, or if there are significant seeing changes. In these cases a flat-field correction may prove important. Given the extremely high count levels of the science frames that are obtained during a transit, very large numbers of well exposed flat-field images are needed such that the photon noise levels per-pixel in the combined flat-field is comparable to the integrated photon noise levels per pixel in the science frames. Thus, be sure to obtain as many flat-field and bias images as possible, as it is unlikely taking one or two flat-field images would prove useful when a time-series dataset is aiming for high photometric precisions measuring a transit depth over perhaps hundreds or thousands of images.

- The science exposures are flat-fielded, and bad-pixels corrected if desired.
- Cosmic rays are cleaned.
- The spectra center is determined, trace defined, and 1D spectra extracted.
In a 2D spectral image, the center of the PSF at each pixel along the cross-dispersion direction is determined, called the trace. The background region is then defined and the counts in the cross-dispersion direction are then summed in an aperture of a given size along the trace to add up the total counts for each wavelength-pixel in the spectrum, typically subtracting the background. The optimal aperture size and optimal background region have to be explored to optimise the time-series photometry at later stages.
- A wavelength solution is determined.
Typically, arc lamp frames are gathered and the wavelength of specific emission lines are identified, which then provides a direct wavelength-to-pixel mapping. In the case of transit spectroscopy, stellar absorption features can also provide a direct and unambiguous identification of the wavelength (for example the Na D lines in optical spectra).

With space-based transit spectroscopy, one can proceed more or less directly from spectral extraction to fitting light curves. In the case of ground-based multi-object spectroscopy (MOS), the spectra of two or more stars must be extracted as a reference star is needed to correct each spectroscopic channel for the effects of Earth's atmosphere. The method of MOS is essentially an extension of differential photometry, and was initially applied by [Bean et al. \(2010\)](#) to observe the transmission spectra of GJ1214b with VLT FORS2. In MOS observations, the spectra of two or more stars are obtained using typically a mask or longslit, with the slit sizes specifically chosen to be very wide such that slit light losses are minimized or eliminated all together (see Fig. 12). Sizes of 10''+ or more are often used, with an example of [Nikolov et al. \(2016\)](#) using 22'' \times 90'' sizes slits on VLT FORS2. The target and reference spectra must then be accurately wavelength calibrated, such that light curves at the same wavelengths can be binned and constructed for use in

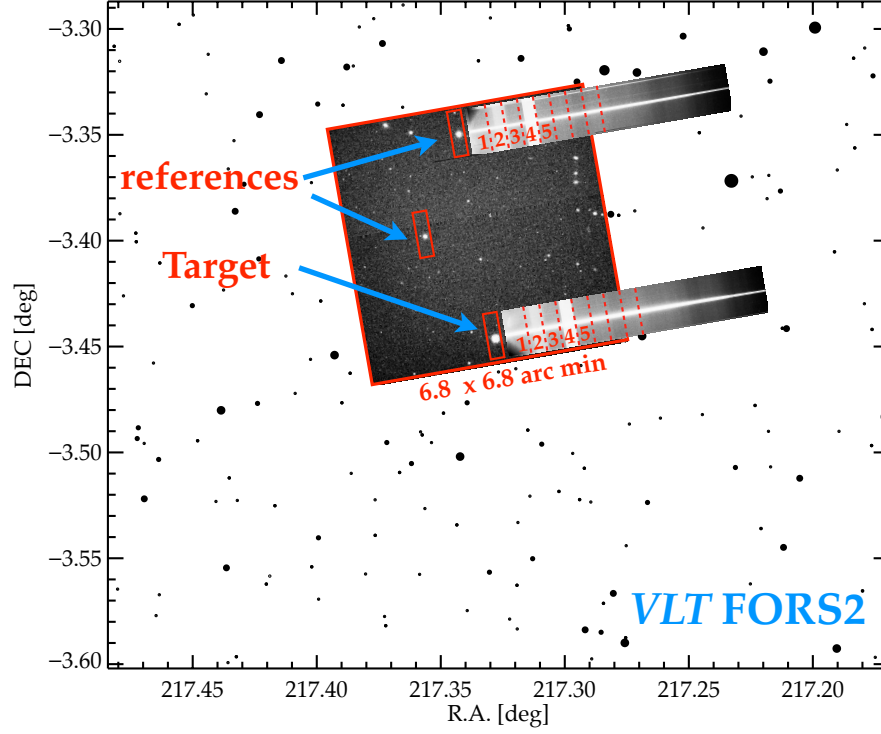


Fig. 12 Illustration of ground-based multi-object differential spectroscopy. Shown is the field of view of VLT FORS2 instrument along with the surrounding field of WASP-6b, overlaid with an acquisition image and a spectroscopic image. The red rectangles on the acquisition image show the large slits as they are projected on the sky, which encompass the target and a number of nearby reference stars. The numbered rectangles depict example wavelength bins for the target and reference star. Fig. courtesy of N. Nikolov.

differential photometry (see Fig. 13). In principle, the reference star should have all the adverse effects from Earth's atmosphere also encoded in the light curves including seeing variations, transparency variations, and changing atmospheric extinction. Dividing the target star light curve by the reference star then largely subtracts out these features. In practice, other effects must also be dealt with such as instrument flexure and pointing drifts.

3.3 *Pre-light curve fitting*

For most areas of astronomical observations, the data reduction steps would largely stop here and the scientific analysis would begin, though with transmission or emission spectroscopy of exoplanets, the job is just partially complete. The very impor-

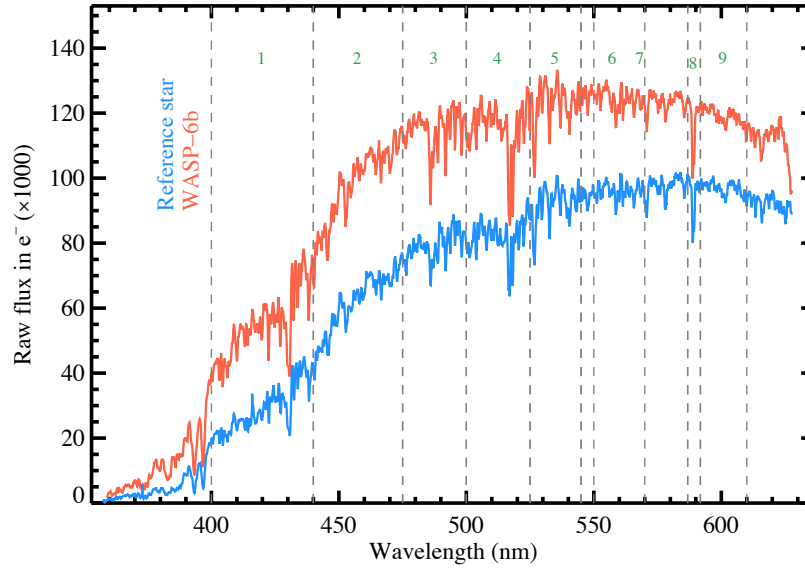


Fig. 13 Stellar spectra of WASP-6A and a target star, along with the bins used to create the spectroscopic channels transit light curves. Fig. courtesy of N. Nikolov.

tant steps of fitting the transit light curves (along with systematic trends) for each spectroscopic channel still need to be performed. In most cases, the light curve fitting stage takes the most time and effort and it remains a non-trivial process which must be handled with care.

There are several important initial steps which need to be taken before fitting transit light curves:

- Calculate accurate time stamps for the time series images.

Very high quality light curves can often have quantities like the central transit time measured to precisions of seconds or better, and other studies will often use the measured quantities to look for transit time variations or followup an exoplanet at a later date, making accurate time stamps very important. Indeed, care must be taken when combining different datasets from different observatories, as it is often hard to know exactly what clock standard was used. The commonly used Julian Date (JD) can be specified in several different time standards which are often unreported, complicating timing studies. Fortunately, [Eastman et al. \(2010\)](#) provides a useful tool to calculate the Barycentric Julian Date in the Barycentric Dynamical Time (BJD_{TDB}) standard, which has become a common practice in the exoplanet literature (<http://astrutils.astronomy.ohio-state.edu>). With an accurate time-stamp, the projected separation between the planet and star, s , as a function of the orbital phase, ϕ , can be calculated as,

$$s(\phi) = \frac{a}{R_{star}} \sqrt{[\sin(2\pi\phi)]^2 + [\cos(i) \cos(2\pi\phi)]^2} \quad (8)$$

where a is the semi-major axis and i is the inclination of the orbit. $s(\phi)$ is a quantity provided as input to widely used transit models such as [Mandel & Agol \(2002\)](#).

- Align the spectra onto a common wavelength/pixel grid.
Spectra are often seen to exhibit non-trivial shifts on the detector during the time series sequence. These shifts need to be accounted for if the spectra are to be placed on a common wavelength grid such that spectral bins can accurately be extracted. Without applying such a correction, fixed pixel bins of the spectral time series could contain a mix of wavelengths as the light from neighbouring pixels would contaminate the bin and degrade the light curves. Shifts between spectra can be easily measured using cross correlation procedures, and the spectra can be interpolated onto a common scale.
- Calculate limb darkening coefficient for the wavelength bin of interest.
Limb darkening is an essential component determining the shape of a transit light curve, enhancing the U-shape of transit light curves due to the non-uniform flux profile across stellar discs. Thus, an accurate treatment of stellar limb darkening is critical when deriving precise planetary radii and measuring transmission spectra. The effects of limb darkening are typically parameterized using a specified functional form (or law), and theoretical limb-darkening coefficients (LDCs) are calculated using stellar models (e.g. [Claret 2000](#)). The most commonly used in exoplanetary transit work are:

the linear law

$$\frac{I(\mu)}{I(1)} = 1 - u(1 - \mu), \quad (9)$$

the quadratic law

$$\frac{I(\mu)}{I(1)} = 1 - a(1 - \mu) - b(1 - \mu)^2, \quad (10)$$

the three-parameter non-linear law,

$$\frac{I(\mu)}{I(1)} = 1 - c_2(1 - \mu) - c_3(1 - \mu^{3/2}) - c_4(1 - \mu^2), \quad (11)$$

and the four-parameter non-linear law

$$\frac{I(\mu)}{I(1)} = 1 - c_1(1 - \mu^{1/2}) - c_2(1 - \mu) - c_3(1 - \mu^{3/2}) - c_4(1 - \mu^2), \quad (12)$$

where $I(1)$ is the intensity at the centre of the stellar disk, $\mu = \cos(\theta)$ (where θ is the angle between the line of sight and the emergent intensity), while u , a , b , and c_n are the LDCs. These laws can all be used along with the analytical transit light models of [Mandel & Agol \(2002\)](#) or [Kreidberg \(2015\)](#).

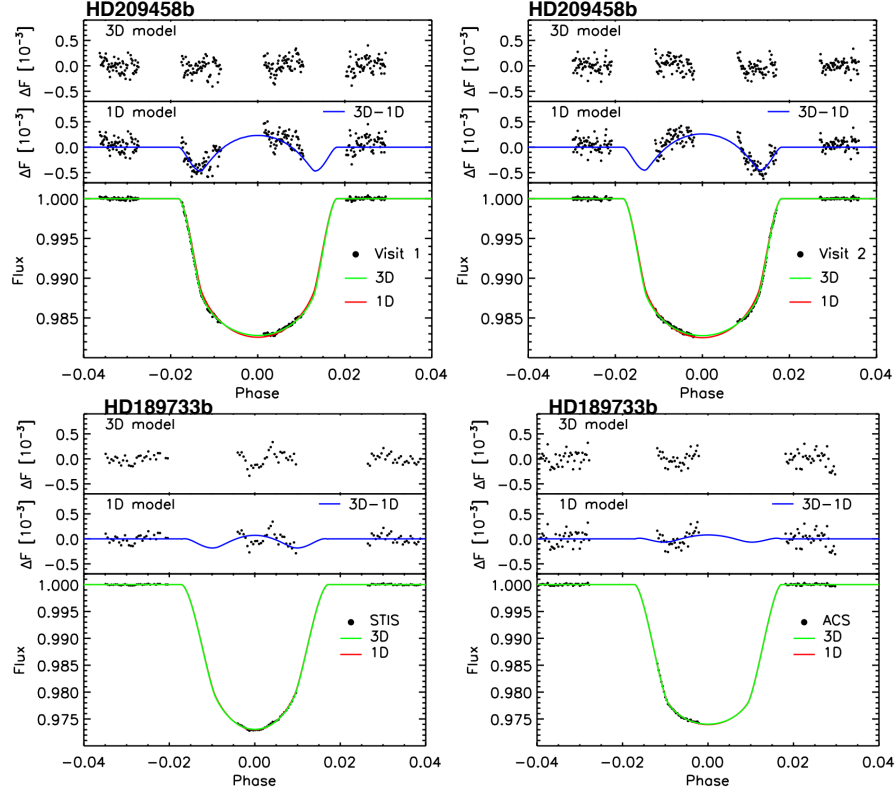


Fig. 14 HST transit light curves of HD 209458b and HD 189733b compared to transit model fits using 1D and 3D models (adapted from [Hayek et al. 2012](#)). (Top) For HD 209458b 1D models are unable to fully reproduce the transit shape, leading to a characteristic “w” shaped residual as seen in the middle panels for each fit and 3D stellar models do a better job of fitting the transit. (Bottom) The 1D models perform better for HD 189733b.

Fitting for LDC from the transit light curves is widely used, with the quadratic law most often adopted. However, there are degeneracies in fitting for the coefficients and without a proper treatment unphysical stellar intensities can result which can bias the results. This can happen especially for grazing transits as the full stellar disk (and its intensity profile) is not sampled during the transit. In addition, simple limb darkening laws can also do a poor job of reproducing a real stellar intensity profile. For many transmission spectral applications, theoretical stellar models have proven adequate for many transit light curve fits (e.g. [Sing et al. 2011](#)) and the latest 3D models (see Fig. 14 and [Hayek et al. 2012](#); [Magic et al. 2015](#)) have improved upon many of the deficiencies seen in earlier 1D models ([Knutson et al., 2007a](#); [Sing et al., 2008](#)). For transit spectroscopy, it is often recommended to fix the limb-darkening coefficients to their theoretical values,

and inspect the fitted residuals to see how well the stellar models are performing, and fit for the coefficients if necessary.

3.4 Light curve fitting

When fitting for a spectroscopic transit or eclipse dataset, the first fits one typically performs is on the wavelength-integrated flux of the spectrum, which is called the white-light curve. The white-light curve fit helps provide the overall system parameters such as i , a/R_{star} and center of transit time T_0 as well as the average transit depth across the wavelength range of the spectrum.

In most all transit light curves to date, a model of the systematic trends (any non-transit/eclipse related phenomena which affects the light curve) must also be taken into account, whether they are of an instrumental or astrophysical nature. For example, in Spitzer IRAC transit photometry, it has been widely established the intra-pixel sensitivities and pointing jitter cause variations in the photometric light curves which must be modelled and removed (Morales-Calderón et al., 2006; Knutson et al., 2008). For HST STIS data, thermal breathing trends cause the point-spread-function (PSF) to change repeatedly for each 90 minute spacecraft orbit around the Earth, producing corresponding photometric changes in the light curve which results in photometric changes in the light curve (Brown et al., 2001). Systematic errors are often removed by a parameterized deterministic model, where the non-transit photometric trends are found to correlate with a number n of external parameters (or optical state parameters, \mathbf{x}). These parameters describe changes in the instrument or other external factors as a function of time during the observations, and are fit with a coefficient for each optical state parameter, p_n , to model and remove (or detrend) the photometric light curves.

When including systematic trends, the total parameterized model of the flux measurements over time, $f(t)$, can be modelled as a combination of the theoretical transit model, $T(t, \theta)$ (which depends upon the transit parameters θ), the total baseline flux detected from the star, F_0 , and the systematics error model $S(\mathbf{x})$ giving,

$$f(t) = T(t, \theta) \times F_0 \times S(\mathbf{x}). \quad (13)$$

In the case of HST STIS data, external detrending parameters including the 96 minute HST orbital phase, ϕ_{HST} , the X_{psf} and Y_{psf} detector position of the PSF, and the wavelength shift S_λ of the spectra have been identified as optical state parameters (Sing et al. 2011). The optical state parameters must be properly normalized such that they do not contribute in changing the overall average system flux, and in the case of STIS data a fourth-order polynomial with ϕ_{HST} has been shown to sufficiently correct the instrument systematics such that $f(t)$ can be written as,

$$f(t) = T(t, \theta) \times F_0 \times (p_1 \phi_{HST} + p_2 \phi_{HST}^2 + p_3 \phi_{HST}^3 + p_4 \phi_{HST}^4 + 1) \\ \times (p_5 S_\lambda + 1) \times (p_6 X_{psf} + 1) \times (p_7 Y_{psf} + 1). \quad (14)$$

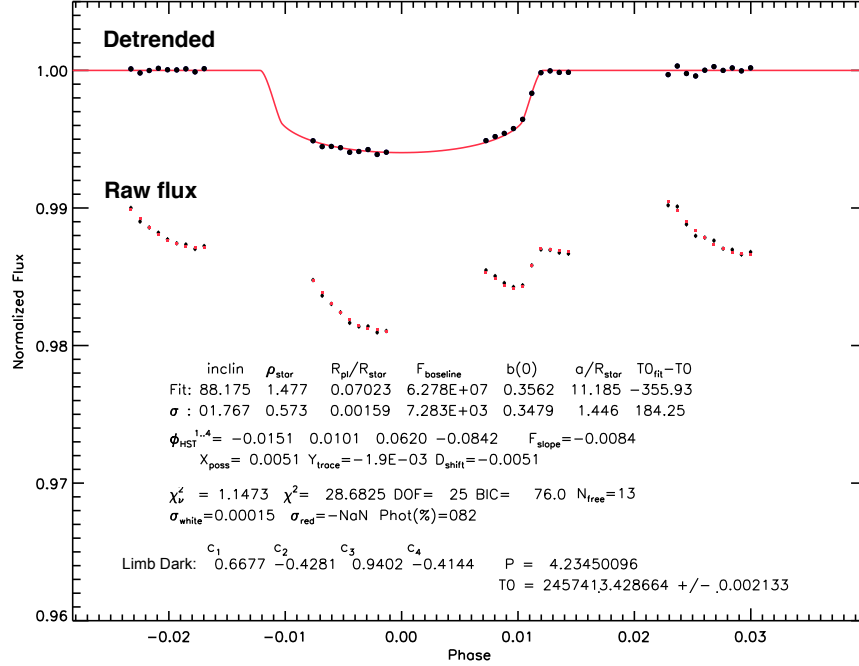


Fig. 15 Example transit light curve minimum χ^2 fit to HST STIS data of HAT-P-26b (Wakeford et al. 2017). Top shows the detrended normalized light data (black points) with the transit light curve model (red line), middle shows the raw flux which includes the instrument systematic trends along with the best-fit model (red points), an arbitrary offset has been applied for clarity. The best-fit model parameters and several statistics of the model are also indicated. In this example, the fit achieves precisions of 82% the theoretical photon noise levels.

Note that the systematics model can also be additive rather than multiplicative as in Eq. 14. Determining what systematic model to use, identifying parameters which successfully detrend light curves, and finding suitable functions while avoiding overfitting remains a large non-trivial challenge when analysing transit light curves. This is especially true if the data collected does not have a significant history and standard practices determined when dealing with high precision photometric time-series measurements. Non-parametric methods have also been developed to model systematic models, and methods such as Gaussian processes (GP) have the benefit of not imposing a specific functional dependence on the optical state vectors (see Gibson et al. 2012a), and have become widely used.

When fitting transit models to the data, typically one begins by finding a minimum χ^2 solution (see Fig. 15) from routines such as the Levenberg-Marquardt (L-M) least squares method (Markwardt, 2009), while Markov chain Monte Carlo techniques (MCMC) methods are useful for deriving robust error estimates that can account for complicated degeneracies between model parameters (Eastman et al., 2013; Foreman-Mackey et al., 2013).

The size of the photometric error bars are a critical, and often overlooked aspect of light curve fitting. Typically, the minimum χ^2 values and best-fit parameters are insensitive to the exact size of the errors (within reason). However, the inferred uncertainties on the best-fit model parameters themselves are dependent upon the size of the photometric errors/uncertainties given. In high-precision time-series photometry, it is often the case that the formal error bars are dominated by photon noise. However, for many datasets photon noise is rarely achieved and can even be factors of a few away from achieving those levels of precision. A common practice is to adopt photon-noise error bars when performing model selection, such that a given model $f(t)$ performance can be compared to the theoretical limit of the data, and a comparison can be made between the performance of different models. However, when a satisfactory model is found, the photometric error bars themselves are rescaled by the standard deviation of the residuals, and the model is re-fit. Alternatively, for methods such as MCMC that optimise the log-likelihood, the photometric/white noise level can be fit as a free parameter itself. Rescaling the error bars in these ways helps take into account noise sources that are difficult to account for in standard pipeline reduction routines, and the final uncertainties will be underestimated if this step (or a similar procedure) is not taken, unless of course photon noise precisions were achieved. In addition, the presence of time-correlated red noise must also be considered, with the binning technique (Pont et al., 2006) and wavelets (Carter & Winn, 2009) two recommended methods. With the photometric error bars set to realistic values, and red noise properly handled, MCMC routines (e.g. Eastman et al. 2013; Foreman-Mackey et al. 2013.) can then be run to provide the full posterior distribution and marginalised parameter uncertainties (see Fig. 16).

After the white light curve is fit, the spectroscopic channels are then determined and transmission or emission spectra constructed. During this stage, it is typically only the transit or eclipse depth that is allowed to vary along with the systematics model in the fits. All other parameters tend to be fixed to those values adopted for the white light curve, as they are not expected to vary across spectroscopic channels. This includes the semi major axis a , orbital inclination i and transit/eclipse mid-time. An important exception is the limb-darkening coefficients, which as noted above must be carefully determined for each spectroscopic channel individually as they are wavelength-dependent.

Below are a few tips to consider regarding transit observations:

1. Observe whole time series on the same pixel, sub-pixel if possible.
2. Choose a detector setting (e.g. gain) to get as many counts as reasonably possible per image in order to improve the relative photometric precision.
3. Readnoise is almost never important, as we tend to observe bright targets, so the error budget is dominated by photon noise.
4. Red noise is always important to consider.
5. For MOS, wide slits/apertures are needed to minimise differential slit losses between the target and reference stars.
6. Have a uniform detector.
7. Be mindful of detector electronics which can introduce noise.

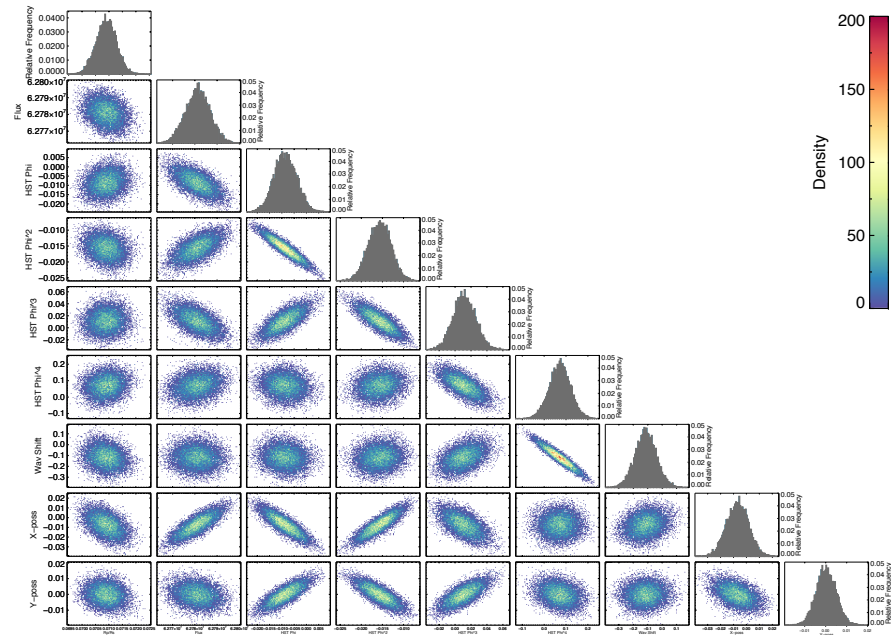


Fig. 16 Example MCMC posterior distribution using of a transit light curve model fit to HST STIS HAT-P-26b data (Wakeford et al., 2017).

8. Get a long enough baseline before and after the transit/eclipse to properly measure the depth.
9. As much as possible, have the out-of-transit/eclipse baseline sample similar systematics to those in-transit/eclipse.
10. Ingress and egress are not very useful to measure the transit/eclipse depth but are needed to measure a/R_{star} , T_0 , and the inclination.
11. Avoid or correct for non-linearities in the detector.
12. Reference stars need to be as similar as possible to the target in type & magnitude (preferably within 1 mag, and spectral sub-type).
13. Near-IR is hard from the ground, due to terrestrial opacity sources such as water, but not impossible.
14. Philosophy differs in flat-fielding (I suggest gathering 100's, test to see if they improve things or not).
15. Cosmic Rays are important.
16. Visualise your time series data (e.g. with a movie) to see all the ways your spectra/photometry changes in time.
17. Be wary of hidden companions that can dilute the flux of the brighter star you're interested in.
18. Be wary of unphysical results.

4 Interpreting a Transmission Spectra

In the following section, an analytic transmission spectra formula is derived from first principles. Details of this derivation can be found across [Fortney et al. \(2005\)](#), [Lecavelier des Etangs et al. \(2008\)](#), [de Wit & Seager \(2013\)](#), [B  tr  mieux & Swain \(2017\)](#) and [Heng & Kitzmann \(2017\)](#). Given that a transmission spectrum is not a typical astrophysical measurement, the derivation helps to illustrate how the spectrum depends upon several key parameters (such as the temperature and molecular abundances), what quantities can be derived from a transmission spectra, and the nature of modelling degeneracies.

4.1 Analytic Transmission Spectrum Derivation

The flux blocked during transit including the planet and its atmosphere is given by the ratio of the areas,

$$\frac{\Delta f}{f} = \frac{\pi R_{pl}^2 + A}{\pi R_{star}^2}, \quad (15)$$

where A is the effective area of the annular region of the atmosphere observed during transit. The contribution of the atmosphere, A , is calculated by integrating the absorptivity of the atmosphere from a reference planetary radius, R_{pl} , up to the top of the atmosphere along the radial coordinate direction r' and is given by,

$$A = \int_{R_{pl}}^{\infty} (1 - T) 2\pi r' dr' \quad (16)$$

where T is the transmittance which is the fraction of radiation that is transmitted through a given layer of atmosphere. The transmittance is related to the optical depth τ using the Beer-Lambert law,

$$T = e^{-\tau}, \quad (17)$$

and the optical depth in turn can also be written in terms of the cross section of absorbing species $\sigma_{abs}(\lambda)$, its number density n_{abs} , and integrated along the slant transit geometry (direction \hat{x}),

$$\tau = \int_{-\infty}^{+\infty} \sigma_{abs}(\lambda) n_{abs} dx, \quad (18)$$

$$T = e^{-\int_{-\infty}^{+\infty} \sigma_{abs}(\lambda) n_{abs} dx}. \quad (19)$$

As the number density of an atmosphere drops with altitude radially (direction \hat{r}), a simplifying approximation can be made by assuming the atmosphere is isothermal with temperature T , an ideal gas with pressure $P = k_B \rho T / \mu$, where ρ is the density, and in hydrostatic balance,

$$dP = -\rho g dr. \quad (20)$$

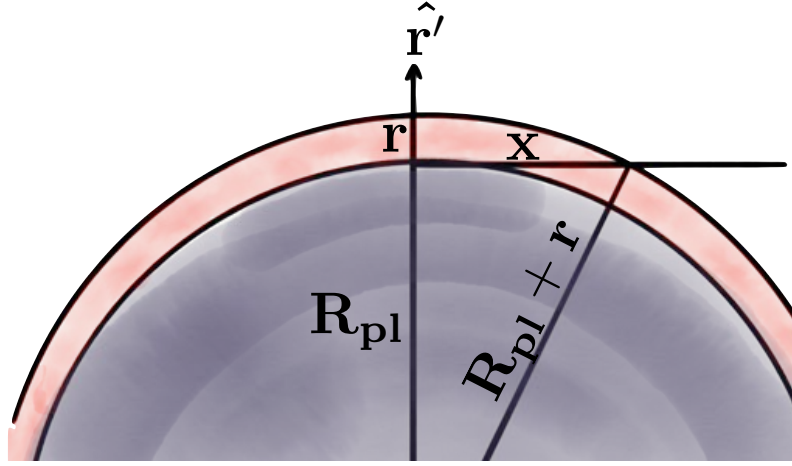


Fig. 17 Illustration of the transit geometry. The bulk radius of the planet, R_{pl} (grey) is illustrated along with an atmospheric layer (red) of thickness, r . Stellar light passes in slant transit geometry from the terminator through the atmospheric layer a distance x . The radial coordinate \hat{r} is also indicated with its origin at the planet center.

Substituting ρ from the ideal gas law and integrating Eq. 20 then gives the Barometric formula which relates the pressure between two points (labeled here as 0 and 1) with the altitude difference, $P_1 = P_0 e^{-r/H}$, and pressure scale height H or equivalently the number density between two altitude points,

$$n_1 = n_0 e^{-r/H}. \quad (21)$$

Typically, the absorbing species in a transmission spectra is a minor component of the gas, so we can relate the mixing ratio of the absorbing minor species, ξ_{abs} , to the total gas number density, by $n_{abs} = n_0 \xi_{abs}$. Substituting Eq. 21 into Eq. 18 and evaluating the optical depth at the reference planetary radius and pressure (R_{pl} , P_0) gives,

$$\tau_0 = \xi_{abs} \sigma_{abs}(\lambda) \int_{-\infty}^{+\infty} \frac{P_0}{k_B T} e^{-r'/H} dx, \quad (22)$$

where we have made the assumption that the cross section $\sigma_{abs}(\lambda)$ does not depend upon the atmospheric pressure. The \hat{x} and \hat{r} coordinates can be related by the Pythagorean theorem (see Fig. 17),

$$(R_{pl} + r)^2 = R_{pl}^2 + x^2 \quad (23)$$

$$x^2 = 2R_{pl}r + r^2, \quad (24)$$

and further simplified assuming planetary radius is much larger than the atmospheric altitude ($R_{pl} \gg r$) which gives

$$r = \frac{x^2}{2R_{pl}}. \quad (25)$$

Substituting r into Eq. 22 gives,

$$\tau_0 = \xi_{abs} \sigma_{abs}(\lambda) \int_{-\infty}^{+\infty} \frac{P_0}{k_B T} e^{-x^2/2R_{pl}H} dx. \quad (26)$$

The integral can be analytically evaluated as, $\int_{-\infty}^{+\infty} e^{-u^2} du = \sqrt{\pi}$, so the reference optical depth becomes,

$$\tau_0 = \xi_{abs} \sigma_{abs}(\lambda) \frac{P_0}{k_B T} \sqrt{2\pi R_{pl}H}. \quad (27)$$

From Eq. 27, it can be seen that the optical depth depends on the pressure (i.e. $\tau \propto P$), and again using the Barometric formula the optical depth at an arbitrary pressure P can be written as,

$$\tau = \xi_{abs} \sigma_{abs}(\lambda) \frac{P}{k_B T} \sqrt{2\pi R_{pl}H}. \quad (28)$$

Before we can evaluate Eq. 16, we need a relation between the the radial coordinate \hat{r}' and optical depths τ and $d\tau$. Using the Barometric formula in terms of pressure, and the fact that the optical depth is proportional to pressure gives,

$$\frac{\tau}{\tau_0} = \frac{P}{P_0} = e^{-r/H}, \quad (29)$$

$$\tau = \tau_0 e^{-r/H}, \quad (30)$$

the altitude difference, r , is then related to the reference radius of the planet and radial coordinate r' as $r = r' - R_{pl}$, thus

$$\tau = \tau_0 e^{-(r' - R_{pl})/H}, \quad (31)$$

$$\ln\left(\frac{\tau}{\tau_0}\right) = -\frac{r'}{H} + \frac{R_{pl}}{H}, \quad (32)$$

$$r' = R_{pl} - H \ln \frac{\tau}{\tau_0}, \quad (33)$$

and

$$dr' = -\frac{H}{\tau} d\tau. \quad (34)$$

Substituting these values r' of dr' into Eq. 16 along with Eq. 28 and Eq. 17 then gives,

$$A = 2\pi \int_{\tau_0}^0 (1 - e^{-\tau}) \left(R_{pl} - H \ln \frac{\tau}{\tau_0} \right) \left(-\frac{H}{\tau} d\tau \right), \quad (35)$$

where the integration limits have also been converted into the appropriate optical depth limits. After a slight rearrangement, Eq. 35 can be written

$$A = 2\pi HR_{pl} \int_0^{\tau_0} \left(\frac{1 - e^{-\tau}}{\tau} \right) \left(1 + \frac{H}{R_{pl}} \ln \frac{\tau_0}{\tau} \right) d\tau, \quad (36)$$

which can then be further simplified assuming $H/R_{pl} \ll 1$ so a term can be neglected to give,

$$A = 2\pi HR_{pl} \int_0^{\tau_0} \left(\frac{1 - e^{-\tau}}{\tau} \right) d\tau. \quad (37)$$

The integral can be found in [Chandrasekhar \(1960\)](#),

$$E_1 = -\gamma - \ln \tau_0 + \int_0^{\tau_0} \left(\frac{1 - e^{-\tau}}{\tau} \right) d\tau, \quad (38)$$

where γ is the Euler-Mascheroni constant ($\gamma = 0.577215664901\dots$) and E_1 is an exponential integral which is a transcendental function. Thus, Eq. 37 becomes,

$$A = 2\pi HR_{pl} [E_1 + \gamma + \ln \tau_0]. \quad (39)$$

During a transit, we measure the transit-depth radius of the combined planet and atmosphere. Thus to relate 39 to the transit radius, we can set the measured transit depth altitude r_{eq} so it produces the same absorption depth as the planet with its translucent atmosphere occulting area, A , giving,

$$A = 2\pi R_{pl} r_{eq} = 2\pi HR_{pl} [E_1 + \gamma + \ln \tau_0], \quad (40)$$

$$r_{eq} = H [E_1 + \gamma + \ln \tau_0]. \quad (41)$$

As τ_0 is the optical depth an arbitrary reference pressure-altitude level, we can set this value to be very large ($\tau_0 \gg 1$) to use the limit where $E_1 \rightarrow 0$ as $\tau_0 \rightarrow \infty$,

$$r_{eq} = H [\gamma + \ln \tau_0]. \quad (42)$$

Eq. 42 can then be rearranged and the radius converted to optical depth (Eq. 34) to figure out the equivalent optical depth τ_{eq} where the transmission spectrum becomes optically thick in slant transit geometry and corresponds to the measured transit-depth radius giving,

$$r_{eq}/H = \gamma + \ln \tau_0, \quad (43)$$

$$e^{-r_{eq}/H} = \tau_{eq}/\tau_0 = e^{-\gamma - \ln \tau_0}, \quad (44)$$

$$\tau_{eq}/\tau_0 = e^{-\gamma}/\tau_0, \quad (45)$$

$$\tau_{eq} = e^{-\gamma} = 0.561459. \quad (46)$$

[Lecavelier des Etangs et al. \(2008\)](#) first derived τ_{eq} numerically, where $\tau_{eq} = 0.56$ is seen to be an accurate approximation (given the terms we have neglected) for most

planetary atmospheres as long as ($30 > R_{pl}/H > 300$). Finally, we can substitute Eq. 46 and Eq. 27 into Eq. 42 to give,

$$r_{eq} = H \left[-\ln \tau_{eq} + \ln \left(\xi_{abs} \sigma_{abs}(\lambda) \frac{P_0}{k_B T} \sqrt{2\pi R_{pl} H} \right) \right], \quad (47)$$

$$r_{eq} = H \left[\ln \left(\frac{\xi_{abs} \sigma_{abs}(\lambda) P_0}{\tau_{eq}} \sqrt{\frac{2\pi R_{pl} H}{k_B^2 T^2}} \right) \right], \quad (48)$$

and r_{eq} relabelled as $z(\lambda)$ which then derives the [Lecavelier des Etangs et al. \(2008\)](#) transmission spectrum formula,

$$z(\lambda) = H \ln \left(\frac{\xi_{abs} \sigma_{abs}(\lambda) P_0}{\tau_{eq}} \sqrt{\frac{2\pi R_{pl}}{k_B T \mu g}} \right). \quad (49)$$

4.2 Analytic Transmission Spectrum Applications

The first application of Eq. 49 was to interpret the transmission spectrum of HD 189733b from [Pont et al. \(2008\)](#) in which atmospheric haze on an exoplanet was first discovered. If the cross section $\sigma_{abs}(\lambda)$ is known, then the altitude difference between two wavelengths, dz , allows the pressure scale height H to be directly measured, which directly leads from Eq. 49 to,

$$T = \frac{\mu g}{k_B} \left(\frac{d \ln \sigma}{d \lambda} \right)^{-1} \frac{dz(\lambda)}{d \lambda}. \quad (50)$$

This temperature measurement will be accurate in the case where the absorbing species in the transmission spectra has been robustly identified, such as is often the case for Na, K, or H₂O, and when the mean molecular weight of the atmosphere is also known. Thus, the terminator temperatures in hot Jupiters can often be accurately measured, given the atmosphere is H/He dominated; though that may not be the case for super-Earths which could have much heavier non-H/He secondary atmospheres.

For HD 189733b, the slope of the transmission spectra indicated a scattering slope, and the cross section could be assumed to follow a power law of index α , such that $\sigma = \sigma_0(\lambda/\lambda_0)^\alpha$. In this case,

$$\alpha T = \frac{\mu g}{k_B} \frac{d R_{pl}(\lambda)}{d \ln \lambda}, \quad (51)$$

making the transmission spectrum slope proportional to the product αT . In the case of pure Rayleigh scattering, $\alpha=-4$ and the temperature can be derived, though in general if the pure Rayleigh scattering is not apparent, then the constrained quan-

tity will be αT and a degeneracy will exist between the power law index and the atmospheric temperature.

Eq. 49 can be used to straightforwardly make an entire optical transmission spectrum for a hot Jupiter, given that theoretical models have shown a typical hot Jupiter (~ 1200 K) will be dominated by Na, K, and Rayleigh scattering (Seager & Sas-selov, 2000; Hubbard et al., 2001; Brown, 2001). Na and K are both doublets, so by including only four absorption lines and a scattering component, the majority of an hot Jupiter optical transmission spectrum can be modelled.

For largely clear atmospheres, Na and K can both exhibit large pressure-broadened wings which will dominate the optical opacity. These wings can be calculated ana-lytically using a Voigt line profile, $H(a, u)$, and statistical theory, which predicts the collision-broadened alkali line shapes will vary with frequency ν as $(\nu - \nu_0)^{-3/2}$ outside of an impact region, which lies between the line centre frequency ν_0 and a detuning frequency $\Delta\sigma$ away from ν_0 .

Within the impact region, the cross-sections for both the sodium and potassium doublets can then be calculated following Burrows et al. (2000) and Iro et al. (2005) as,

$$\sigma(\lambda) = \frac{\pi e^2}{m_e c} \frac{f}{\Delta\nu_D \sqrt{\pi}} H(a, u), \quad (52)$$

where f is the absorption oscillator strength of the spectral line, m_e is the mass of the electron, e the electron charge. The Voigt profile $H(a, u)$ is defined in terms of the Voigt damping parameter a and a frequency offset u . The frequency offset is calculated as $u = (\nu - \nu_0)/\Delta\nu_D$, where $\Delta\nu_D$ is the Doppler width given by $\Delta\nu_D = \nu_0/c \sqrt{2kT/\mu_{\text{Na,K}}}$, with c the speed of light and $\mu_{\text{Na,K}}$ the mean molecular weight of sodium or potassium. The damping parameter is given by $a = \Gamma/(4\pi\Delta\nu_D)$, where the transition rate Γ is calculated following

$$\Gamma = \gamma + \Gamma_{\text{col}}, \quad (53)$$

where γ is the spontaneous decay rate and Γ_{col} is the half-width calculated from classical impact theory. Assuming a Van der Waals force gives,

$$\Gamma_{\text{col}} = 0.071(T/2000)^{-0.7} \text{ cm}^{-1} \text{ atm}^{-1} \quad (54)$$

for Na and

$$\Gamma_{\text{col}} = 0.14(T/2000)^{-0.7} \text{ cm}^{-1} \text{ atm}^{-1} \quad (55)$$

for K (Burrows et al., 2000; Iro et al., 2005).

Outside of the impact region, the $(\nu - \nu_0)^{-3/2}$ power-law line shape is truncated using an exponential cutoff term of the form $e^{-qh(\nu - \nu_0)/kT}$, where h is Planck's constant and q a parameter of order unity, to prevent the line wing opacity from becoming overly large at large frequency separations. The detuning frequency, $\Delta\sigma$, can be estimated from Burrows et al. (2000) using

$$\Delta\sigma = 30(T/500 \text{ K})^{0.6} \text{ cm}^{-1}. \quad (56)$$

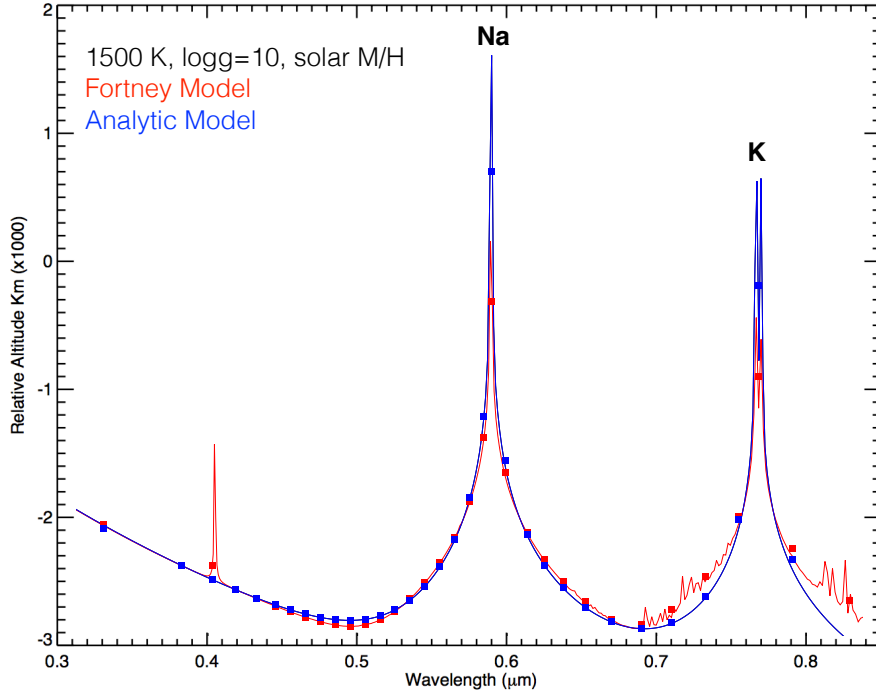


Fig. 18 Comparison between an analytic transmission spectrum model for a 1500 K hot Jupiter calculated using Eq. 49 (blue) and a model from Fortney et al. (2010).

for the sodium doublet and

$$\Delta\sigma = 20(T/500 \text{ K})^{0.6} \text{ cm}^{-1}. \quad (57)$$

for the potassium doublet.

The wavelength-dependent total cross sections of the sodium or potassium D1 and D2 doublet can then be summed together, $\sigma(\lambda)_{Na,K} = \sigma(\lambda)_{D1} + \sigma(\lambda)_{D2}$, and the sodium and potassium opacities can also be summed together along with their abundances into Eq. 49 as,

$$\xi_{abs}\sigma_{abs} = \xi_{Na}\sigma_{Na} + \xi_K\sigma_K. \quad (58)$$

Finally, a Rayleigh scattering component can also be added to the alkali lines, given that $\sigma_0 = 2.52 \times 10^{-28} \text{ cm}^2$ at $\lambda_0 = 750 \text{ nm}$ for molecular hydrogen and for a hot Jupiter $\xi_{H_2} \sim 1$.

A comparison between the analytic transmission spectrum (Eq. 49) and a numerical model from Fortney et al. (2010) is shown in Figure 18. The analytic model reproduces the Na and K lines profiles well, and certainly better than the accuracy of any transmission spectral data to date. The small differences seen are mainly due to the inclusion of molecules such as H_2O in the Fortney et al. (2010) model, which

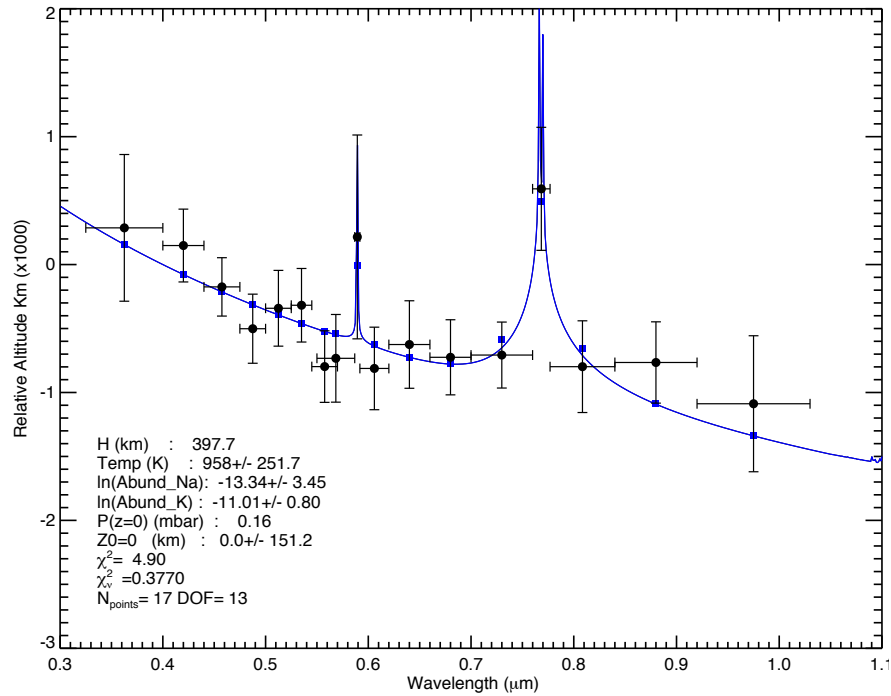


Fig. 19 Analytic atmospheric model fit of the WASP-6b HST transmission spectrum from [Nikolov et al. \(2015\)](#). Four parameters are fit, the temperature, Na and K abundances, and a baseline reference planet radius. The best-fit parameters and χ^2 statistics are indicated on the plot.

can be seen as weak lines near the K doublet, and the inclusion of weaker Na/K lines (e.g. 0.4 μm) which have not been added in this example analytic model.

The analytic transmission spectrum (Eq. 49) can easily be used to fit data in a retrieval model exercise (e.g. [Sing et al. 2015](#)), which given the few parameters and analytic nature is very fast making it highly conducive to Markov chain Monte Carlo techniques (MCMC). In Fig. 19 the WASP-6b optical HST data from [Nikolov et al. \(2015\)](#) is well fit using only four parameters: the abundances of Na and K, as well as the temperature and baseline planetary radius.

In general, molecular species can also be modeled with the analytic transmission spectrum (Eq. 49) as well, in this case the number of spectral lines jumps from four up to 10^9 or 10^{10} depending on the line list and species in question, which dramatically increases the computational burden. Nevertheless, even if one uses a fully numerical tool to calculate and model transmission spectra, it is a good idea to keep Eq. 49 in mind such that a physical intuition can be preserved.

A further consequence of Eq. 49 is that abundance ratios can be very precisely measured in a transmission spectrum. This follows from measuring the altitude difference in the spectra between the two (or more) wavelengths where the two species dominate. For example, taking the difference in altitudes between the transmission

spectra at the Na core wavelengths, z_{Na} , and potassium core wavelengths z_K ,

$$z_{Na} - z_K = H \ln \left(\frac{\xi_{Na} \sigma_{Na}(\lambda) P_0}{\tau_{eq}} \sqrt{\frac{2\pi R_{pl}}{k_B T \mu g}} \right) - H \ln \left(\frac{\xi_K \sigma_K(\lambda) P_0}{\tau_{eq}} \sqrt{\frac{2\pi R_{pl}}{k_B T \mu g}} \right), \quad (59)$$

which can be simplified to,

$$\frac{z_{Na} - z_K}{H} = \ln \left(\frac{\xi_{Na} \sigma_{Na}(\lambda) P_0}{\tau_{eq}} \right) - \ln \left(\frac{\xi_K \sigma_K(\lambda) P_0}{\tau_{eq}} \right), \quad (60)$$

$$\frac{z_{Na} - z_K}{H} = \ln(\xi_{Na} \sigma_{Na}(\lambda)) - \ln(\xi_K \sigma_K(\lambda)), \quad (61)$$

$$e^{\frac{z_{Na} - z_K}{H}} = \frac{\xi_{Na} \sigma_{Na}(\lambda)}{\xi_K \sigma_K(\lambda)}, \quad (62)$$

$$\frac{\xi_{Na}}{\xi_K} = \frac{\sigma_K}{\sigma_{Na}} \exp \left(\frac{z_{Na} - z_K}{H} \right). \quad (63)$$

Almost all of the constants cancel, including importantly P_0 and R_{pl} , and the measured transit difference between the wavelengths of the two species directly translates into the abundance ratios between the two species. In the near-future, this aspect of transmission spectroscopy should lead to well measured C/O ratios in planetary atmospheres given the ratios of the dominant species (H_2O , CO_2 , CO , & CH_4) may all be determined, e.g.

$$\frac{\xi_{H_2O}}{\xi_{CO}} = \frac{\sigma_{CO}}{\sigma_{H_2O}} \exp \left(\frac{z_{H_2O} - z_{CO}}{H} \right). \quad (64)$$

with early attempts of this measurement found in [Désert et al. \(2009\)](#) using Spitzer data.

4.3 Transmission Spectrum Degeneracies

An important degeneracy is apparent from Eq. 49 as the transmission spectrum is determined by the quantity of $\xi_{abs} P_0$. In general, the baseline pressure P_0 at the reference planetary radius is not known. Thus, it is typically difficult to measure absolute abundances in a transmission spectrum, which will be limited by the degeneracy between the abundance and baseline pressure. The degeneracy can also be re-cast as a degeneracy between ξ_{abs} and the reference planetary radius R_{pl} . Further discussion of degeneracies can be found in [Benneke & Seager \(2012\)](#) and [Heng & Kitzmann \(2017\)](#).

One way to lift the $\xi_{abs} - P_0$ degeneracy is to identify Rayleigh scattering by molecular H_2 . Models such as those shown in Fig. 18 predict for clear hot Jupiter atmospheres that short-ward of about $0.5 \mu m$, the H_2 molecular scattering should dominate the opacity. If this is the case, then the abundance of H_2 can be well ap-

proximated given $\xi_{H_2} \sim 1$, and the reference pressure P_0 at $z = 0$ can be determined. From Eq. 49, in the H_2 -Rayleigh spectral region, the pressure P_0 at an altitude corresponding to the radius at wavelength λ_0 is

$$P_0 = \frac{\tau_{eq}}{\sigma_0} \sqrt{\frac{k_B T \mu g}{2\pi R_{pl}}}, \quad (65)$$

where σ_0 is the Rayleigh scattering cross section at λ_0 . If P_0 can be determined from this method, the absolute abundances of all species identified in a transmission spectra (including molecular species at longer infrared wavelengths) can then be determined. In practice, hazes and clouds have often been observed to mask the H_2 Rayleigh scattering signatures. However, even if this is the case the short-wavelength region is still an important wavelength region to measure, as this data can constrain the cloud properties and rule out large classes of models, thereby constraining parameter space and limiting the $\xi_{abs} - P_0$ degeneracy.

In addition to the $\xi_{abs} - P_0$ degeneracy, the transmission spectra is also seen from Eq. 49 to scale (to first order) with the pressure scale height $H = k_B T / \mu g$. The H itself can typically be well determined from a well-measured transmission spectra. For hot Jupiter exoplanets which also have a measured mass, the surface gravity g is also known and μ can safely be assumed to be dominated by a H/He mixture leaving just the temperature as the unknown quantity that can be measured from the transmission spectrum. However, for non-gas giant exoplanets the molecular weight of the atmosphere can be unknown to perhaps an order of magnitude or more given atmospheres dominated for example by N_2 , H_2O , or CO_2 are feasible. In addition, it is also more challenging to measure the mass of small exoplanets via the radial velocity method, which can also hinder a precise determination of g . Thus, in these cases there will be a large $T - g - \mu$ degeneracy, and the individual quantities will be difficult to constrain with the transmission spectrum alone.

Acknowledgements David K. Sing acknowledges the support from the meeting organisers for travel and accommodation at the meeting. DKS also gives thanks to Tom Evans, Nikolay Nikolov, Kevin Stevenson, and Hannah Wakeford for the use of several figures. DKS gives further thanks to Aarynn Carter, Tom Evans, Nikolay Nikolov, Jayesh Goyal, Jessica Spake, and Hannah Wakeford for reviewing the manuscript. DKS acknowledges funding from the European Research Council under the European Unions Seventh Framework Programme (FP7/2007-2013)/ERC grant agreement number 336792.

References

- Bailey, J. 2014, [PASA](#), **31**, 043
 Bean, J. L., Miller-Ricci Kempton, E., & Homeier, D. 2010, [Nature](#), **468**, 669
 Benneke, B., & Seager, S. 2012, [ApJ](#), **753**, 100
 B  tr  mieux, Y., & Swain, M. R. 2017, [MNRAS](#), **467**, 2834
 Boss, A. P. 1997, [Science](#), **276**, 1836

- Brown, T. M. 2001, [ApJ](#), **553**, 1006
- Brown, T. M., Charbonneau, D., Gilliland, R. L., Noyes, R. W., & Burrows, A. 2001, [ApJ](#), **552**, 699
- Burrows, A., Budaj, J., & Hubeny, I. 2008, [ApJ](#), **678**, 1436
- Burrows, A., Hubeny, I., Budaj, J., Knutson, H. A., & Charbonneau, D. 2007, [ApJ](#), **668**, L171
- Burrows, A., Marley, M. S., & Sharp, C. M. 2000, [ApJ](#), **531**, 438
- Burrows, A. S. 2014, [Nature](#), **513**, 345
- Carter, J. A., & Winn, J. N. 2009, [ApJ](#), **704**, 51
- Chandrasekhar, S. 1960, Radiative transfer
- Charbonneau, D., Brown, T. M., Latham, D. W., & Mayor, M. 2000, [ApJ](#), **529**, L45
- Charbonneau, D., Brown, T. M., Noyes, R. W., & Gilliland, R. L. 2002, [ApJ](#), **568**, 377
- Charbonneau, D., Allen, L. E., Megeath, S. T., et al. 2005, [ApJ](#), **626**, 523
- Charbonneau, D., Berta, Z. K., Irwin, J., et al. 2009, [Nature](#), **462**, 891
- Claret, A. 2000, *A&A*, **363**, 1081
- Cowan, N. B., & Agol, E. 2011, [ApJ](#), **729**, 54
- Croll, B., Lafreniere, D., Albert, L., et al. 2011, *AJ*, **141**, 30
- Crossfield, I. J. M. 2015, [PASP](#), **127**, 941
- de Mooij, E. J. W., & Snellen, I. A. G. 2009, *A&A*, **493**, L35
- de Wit, J., & Seager, S. 2013, [Science](#), **342**, 1473
- de Wit, J., Wakeford, H. R., Gillon, M., et al. 2016, [Nature](#), **537**, 69
- Deming, D., Seager, S., Richardson, L. J., & Harrington, J. 2005, [Nature](#), **434**, 740
- Deming, D., Wilkins, A., McCullough, P., et al. 2013, [ApJ](#), **774**, 95
- Deming, L. D., & Seager, S. 2017, [JGRE](#), **122**, 53
- Désert, J.-M., Lecavelier des Etangs, A., Hébrard, G., et al. 2009, [ApJ](#), **699**, 478
- Diamond-Lowe, H., Stevenson, K. B., Bean, J. L., Line, M. R., & Fortney, J. J. 2014, [ApJ](#), **796**, 66
- Dragomir, D., Matthews, J. M., Eastman, J. D., et al. 2013, [ApJ](#), **772**, L2
- Eastman, J., Gaudi, B. S., & Agol, E. 2013, [PASP](#), **125**, 83
- Eastman, J., Siverd, R., & Gaudi, B. S. 2010, [PASP](#), **122**, 935
- Espinoza, N., Fortney, J. J., Miguel, Y., Thorngren, D., & Murray-Clay, R. 2017, [ApJ](#), **838**, L9
- Evans, T. M., Aigrain, S., Gibson, N., et al. 2015, *MNRAS*, **451**, 680
- Evans, T. M., Sing, D. K., Kataria, T., et al. 2017, [Nature](#), **548**, 58
- Fletcher, L. N., Orton, G. S., Teanby, N. A., Irwin, P. G. J., & Bjoraker, G. L. 2009, *Icarus*, **199**, 351
- Foreman-Mackey, D., Hogg, D. W., Lang, D., & Goodman, J. 2013, [PASP](#), **125**, 306
- Fortney, J. J. 2005, *MNRAS*, **364**, 649
- Fortney, J. J., Lodders, K., Marley, M. S., & Freedman, R. S. 2008, [ApJ](#), **678**, 1419
- Fortney, J. J., Marley, M. S., Lodders, K., Saumon, D., & Freedman, R. 2005, [ApJ](#), **627**, L69
- Fortney, J. J., Mordasini, C., Nettelmann, N., et al. 2013, [ApJ](#), **775**, 80
- Fortney, J. J., Shabram, M., Showman, A. P., et al. 2010, [ApJ](#), **709**, 1396
- Gibson, N. P., Aigrain, S., Roberts, S., et al. 2012a, *MNRAS*, **419**, 2683

- Gibson, N. P., Nikolov, N., Sing, D. K., et al. 2017, [MNRAS](#), **467**, 4591
- Gibson, N. P., Aigrain, S., Pont, F., et al. 2012b, [MNRAS](#), **422**, 753
- Gillett, F. C., Low, F. J., & Stein, W. A. 1969, [ApJ](#), **157**, 925
- Gillon, M., Triaud, A. H. M. J., Demory, B.-O., et al. 2017, [Nature](#), **542**, 456
- Grillmair, C. J., Burrows, A., Charbonneau, D., et al. 2008, [Nature](#), **456**, 767
- Harrington, J., Hansen, B. M., Luszcz, S. H., et al. 2006, [Science](#), **314**, 623
- Haswell, C. A. 2010, Transiting Exoplanets
- Hayek, W., Sing, D., Pont, F., & Asplund, M. 2012, [A&A](#), **539**, A102
- Haynes, K., Mandell, A. M., Madhusudhan, N., Deming, D., & Knutson, H. 2015, [ApJ](#), **806**, 146
- Helling, C., Woitke, P., & Thi, W. 2008, [A&A](#), **485**, 547
- Heng, K., & Kitzmann, D. 2017, [MNRAS](#), **470**, 2972
- Henry, G. W., Marcy, G. W., Butler, R. P., & Vogt, S. S. 2000, [ApJ](#), **529**, L41
- Hubbard, W. B., Fortney, J. J., Lunine, J. I., et al. 2001, [ApJ](#), **560**, 413
- Hubeny, I., Burrows, A., & Sudarsky, D. 2003, [ApJ](#), **594**, 1011
- Huitson, C. M., Sing, D. K., Vidal-Madjar, A., et al. 2012, [MNRAS](#), **422**, 2477
- Iro, N., Bézard, B., & Guillot, T. 2005, [A&A](#), **436**, 719
- Jensen, A. G., Redfield, S., Endl, M., et al. 2011, [ApJ](#), **743**, 203
- Karkoschka, E., & Tomasko, M. G. 2011, [Icarus](#), **211**, 780
- Knutson, H. A., Charbonneau, D., Allen, L. E., Burrows, A., & Megeath, S. T. 2008, [ApJ](#), **673**, 526
- Knutson, H. A., Charbonneau, D., Noyes, R. W., Brown, T. M., & Gilliland, R. L. 2007a, [ApJ](#), **655**, 564
- Knutson, H. A., Charbonneau, D., Allen, L. E., et al. 2007b, [Nature](#), **447**, 183
- Knutson, H. A., Dragomir, D., Kreidberg, L., et al. 2014, [ApJ](#), **794**, 155
- Konacki, M., Torres, G., Jha, S., & Sasselov, D. D. 2003, [Nature](#), **421**, 507
- Kreidberg, L. 2015, [PASP](#), **127**, 1161
- Kreidberg, L., Bean, J. L., Désert, J.-M., et al. 2014a, [ApJ](#), **793**, L27
- . 2014b, [Nature](#), **505**, 69
- Lecavelier des Etangs, A., Pont, F., Vidal-Madjar, A., & Sing, D. 2008, [A&A](#), **481**, L83
- Lee, E. J., & Chiang, E. 2016, [ApJ](#), **817**, 90
- Line, M. R., Stevenson, K. B., Bean, J., et al. 2016, [AJ](#), **152**, 203
- López-Morales, M., & Seager, S. 2007, [ApJ](#), **667**, L191
- Madhusudhan, N., Amin, M. A., & Kennedy, G. M. 2014, [ApJ](#), **794**, L12
- Magic, Z., Chiavassa, A., Collet, R., & Asplund, M. 2015, [A&A](#), **573**, A90
- Mandel, K., & Agol, E. 2002, [ApJ](#), **580**, L171
- Markwardt, C. B. 2009, in Astronomical Society of the Pacific Conference Series, ed. D. A. Bohlender, D. Durand, & P. Dowler, Vol. 411, 251
- Marley, M. S., Ackerman, A. S., Cuzzi, J. N., & Kitzmann, D. 2013, Clouds and Hazes in Exoplanet Atmospheres, ed. S. J. Mackwell, A. A. Simon-Miller, J. W. Harder, & M. A. Bullock, 367
- Marley, M. S., Gelino, C., Stephens, D., Lunine, J. I., & Freedman, R. 1999, [ApJ](#), **513**, 879
- Mazeh, T., Naef, D., Torres, G., et al. 2000, [ApJ](#), **532**, L55

- Morales-Calderón, M., Stauffer, J. R., Kirkpatrick, J. D., et al. 2006, *ApJ*, **653**, 1454
- Mordasini, C., Alibert, Y., Benz, W., Klahr, H., & Henning, T. 2012, *A&A*, **541**, A97
- Morley, C. V., Fortney, J. J., Marley, M. S., et al. 2012, *ApJ*, **756**, 172
- Nikolov, N., Sing, D. K., Gibson, N. P., et al. 2016, *ApJ*, **832**, 191
- Nikolov, N., Sing, D. K., Burrows, A. S., et al. 2015, *MNRAS*, **447**, 463
- Nugroho, S. K., Kawahara, H., Masuda, K., et al. 2017, ArXiv e-prints, [arXiv:1710.05276 \[astro-ph.EP\]](https://arxiv.org/abs/1710.05276)
- Öberg, K. I., Murray-Clay, R., & Bergin, E. A. 2011, *ApJ*, **743**, L16
- Pollack, J. B., Hubickyj, O., Bodenheimer, P., et al. 1996, *Icarus*, **124**, 62
- Pont, F., Knutson, H., Gilliland, R. L., Moutou, C., & Charbonneau, D. 2008, *MNRAS*, **385**, 109
- Pont, F., Sing, D. K., Gibson, N. P., et al. 2013, *MNRAS*, **432**, 2917
- Pont, F., Zucker, S., & Queloz, D. 2006, *MNRAS*, **373**, 231
- Redfield, S., Endl, M., Cochran, W. D., & Koesterke, L. 2008, *ApJ*, **673**, L87
- Richardson, L. J., Harrington, J., Seager, S., & Deming, D. 2006, *ApJ*, **649**, 1043
- Ridgway, S. T. 1974, *ApJ*, **187**, L41
- Seager, S., & Deming, D. 2010, *ARA&A*, **48**, 631
- Seager, S., & Sasselov, D. D. 2000, *ApJ*, **537**, 916
- Showman, A. P., & Guillot, T. 2002, *A&A*, **385**, 166
- Sing, D. K., & López-Morales, M. 2009, *A&A*, **493**, L31
- Sing, D. K., Vidal-Madjar, A., Désert, J.-M., Lecavelier des Etangs, A., & Ballester, G. 2008, *ApJ*, **686**, 658
- Sing, D. K., Pont, F., Aigrain, S., et al. 2011, *MNRAS*, **416**, 1443
- Sing, D. K., Wakeford, H. R., Showman, A. P., et al. 2015, *MNRAS*, **446**, 2428
- Sing, D. K., Fortney, J. J., Nikolov, N., et al. 2016, *Nature*, **529**, 59
- Snellen, I. A. G., Albrecht, S., de Mooij, E. J. W., & Le Poole, R. S. 2008, *A&A*, **487**, 357
- Spiegel, D. S., Silverio, K., & Burrows, A. 2009, *ApJ*, **699**, 1487
- Sromovsky, L. A., Fry, P. M., & Kim, J. H. 2011, *Icarus*, **215**, 292
- Stevenson, K. B., Désert, J.-M., Line, M. R., et al. 2014, *Science*, **346**, 838
- Stevenson, K. B., Line, M. R., Bean, J. L., et al. 2017, *AJ*, **153**, 68
- Sudarsky, D., Burrows, A., & Hubeny, I. 2003, *ApJ*, **588**, 1121
- Vidal-Madjar, A., Lecavelier des Etangs, A., Désert, J.-M., et al. 2003, *Nature*, **422**, 143
- Vidal-Madjar, A., Désert, J.-M., Lecavelier des Etangs, A., et al. 2004, *ApJ*, **604**, L69
- Vidal-Madjar, A., Sing, D. K., Lecavelier Des Etangs, A., et al. 2011, *A&A*, **527**, A110
- Visscher, C., Lodders, K., & Fegley, Jr., B. 2010, *ApJ*, **716**, 1060
- Wakeford, H. R., & Sing, D. K. 2015, *A&A*, **573**, A122
- Wakeford, H. R., Sing, D. K., Deming, D., et al. 2013, *MNRAS*, **435**, 3481
- Wakeford, H. R., Sing, D. K., Kataria, T., et al. 2017, *Science*, **356**, 628
- Wakeford, H. R., Sing, D. K., Deming, D., et al. 2018, *AJ*, **155**, 29
- Wallace, L., Prather, M., & Belton, M. J. S. 1974, *ApJ*, **193**, 481

- Wong, M. H., Mahaffy, P. R., Atreya, S. K., Niemann, H. B., & Owen, T. C. 2004, [Icarus](#), 171, 153
- Wytenbach, A., Ehrenreich, D., Lovis, C., Udry, S., & Pepe, F. 2015, [A&A](#), 577, A62